nature cancer

Article

https://doi.org/10.1038/s43018-024-00865-3

Evolving cell states and oncogenic drivers during the progression of IDH-mutant gliomas

Received: 18 September 2023

Accepted: 18 October 2024

Published online: 21 November 2024

Check for updates

Jingyi Wu[1,2,3,8], L. Nicolas Gonzalez Castro[2,4,5,6,8], Sofia Battaglia[1,2,3], Chadi A. El Farran[1,2,3], Joshua P. D'Antonio[1,2,3], Tyler E. Miller[1,2,3,4], Mario L. Suvà[2,4] & Bradley E. Bernstein[1,2,3,7]

Isocitrate dehydrogenase (IDH) mutants define a class of gliomas that are initially slow-growing but inevitably progress to fatal disease. To characterize their malignant cell hierarchy, we profiled chromatin accessibility and gene expression across single cells from low-grade and high-grade IDH-mutant gliomas and ascertained their developmental states through a comparison to normal brain cells. We provide evidence that these tumors are initially fueled by slow-cycling oligodendrocyte progenitor cell-like cells. During progression, a more proliferative neural progenitor cell-like population expands, potentially through partial reprogramming of 'permissive' chromatin in progenitors. This transition is accompanied by a switch from methylation-based drivers to genetic ones. In low-grade IDH-mutant tumors or organoids, DNA hypermethylation appears to suppress interferon (IFN) signaling, which is induced by IDH or DNA methyltransferase 1 inhibitors. High-grade tumors frequently lose this hypermethylation and instead acquire genetic alterations that disrupt IFN and other tumor-suppressive programs. Our findings explain how these slow-growing tumors may progress to lethal malignancies and have implications for therapies that target their epigenetic underpinnings.

Diffusely infiltrating gliomas are progressive brain tumors with limited response to therapy and an invariably fatal outcome. The discovery of mutations in isocitrate dehydrogenase (IDH) genes in a subset of these tumors has led to major advances in our understanding of gliomas and their clinical prognostication[1]. IDH-mutant gliomas account for ~25% of adult gliomas, with patients presenting mainly in their third and fourth decades of life[2]. They are subdivided into oligodendrogliomas (with codeletion of chromosomal arms 1p/19q) and astrocytomas (*ATRX* and *P53* mutations)[3]. Although both subtypes have a better prognosis than wild-type (WT) IDH glioblastoma, they nonetheless progress to a high-grade, fatal disease.

Mutations in IDH genes yield a mutant enzyme that produces the oncometabolite D-2-hydroxyglutarate (D-2HG)[4]. D-2HG is a competitive inhibitor of α-ketoglutarate-dependent enzymes, including histone demethylases and ten-eleven DNA demethylases[5]. As a result, IDH-mutant gliomas exhibit a pattern of global DNA hypermethylation, known as the glioma CpG island methylator phenotype[6,7]. Although methylation changes are widespread, specific methylation events have

[1]Department of Cancer Biology, Dana-Farber Cancer Institute, Boston, MA, USA. [2]Gene Regulation Observatory, Broad Institute of MIT and Harvard, Cambridge, MA, USA. [3]Departments of Cell Biology and Pathology, Harvard Medical School, Boston, MA, USA. [4]Department of Pathology and Krantz Family Center for Cancer Research, Massachusetts General Hospital and Harvard Medical School, Boston, MA, USA. [5]Department of Neurology, Brigham and Women's Hospital, Boston, MA, USA. [6]Center for Neuro-Oncology, Dana-Farber Cancer Institute, Boston, MA, USA. [7]The Novo Nordisk Foundation Center for Genomic Mechanisms of Disease, Broad Institute of MIT and Harvard, Cambridge, MA, USA. [8]These authors contributed equally: Jingyi Wu, L. Nicolas Gonzalez Castro. e-mail: bradley_bernstein@dfci.harvard.edu

been proposed as tumorigenic drivers. Methylation of a binding site for the CCCTC-binding factor insulator protein in the *PDGFRA* locus disrupts insulation and results in epigenetic activation of this canonical glioma oncogene[8,9]. In addition, methylation silences the *CDKN2A* tumor suppressor locus[10,11]. The extent to which other methylation changes or downstream effects of D-2HG also contribute to tumor fitness remains an area of active investigation. For example, impaired histone demethylation hinders differentiation of IDH-mutant glioma progenitors[12], while non-cell-autonomous effects of D-2HG can promote T cell dysfunction[13,14]. Furthermore, the observation that DNA hypermethylation is lost as the tumors progress[15] raises the question of how high-grade or recurrent IDH-mutant tumors are sustained in the absence of methylation-dependent drivers.

Single-cell RNA sequencing (scRNA-seq) studies have shed light on the intratumoral heterogeneity of IDH-mutant gliomas, proposing a hierarchy of malignant cell states that mimics normal development, with stem cell-like populations, as well as more differentiated cells[16,17]. The cell state distributions vary across IDH-mutant subtypes and shift as the tumors progress. Single-cell studies of transposase-accessible chromatin by sequencing (scATAC-seq) have provided additional insights, including evidence that hypermethylation of myelination genes contributes to a differentiation block in oligodendrocyte progenitor cell (OPC)-like cells[18] and a role for *ATRX* loss in shaping the accessibility landscape and promoting myeloid cell infiltration in IDH-mutant astrocytomas[19]. Despite this progress, major gaps remain in understanding the molecular underpinnings and physiologic importance of the diverse malignant cell states in IDH-mutant gliomas.

Here, we address outstanding issues regarding the developmental hierarchies and progression of IDH-mutant gliomas through the combination of scATAC-seq, scRNA-seq and organoid models. By profiling de novo ten IDH-mutant gliomas of different World Health Organization (WHO) grades (2–4), integrating our findings with transcriptional and genetic data for primary and recurrent tumors and benchmarking against normal brain cells, we characterize the malignant progenitors and programs that fuel these gliomas. Our analyses support prominent roles for OPC-like and neural progenitor cell (NPC)-like progenitors, with a permissive epigenetic landscape facilitating transitions between these alternate states. Tumor progression is associated with a striking proportional shift toward the more proliferative NPC-like cells, which share gene markers with normal NPCs but appear deficient in neuronal lineage potential. Progression is also accompanied by a global reduction in DNA methylation and the acquisition of genetic copy number alterations (CNAs) affecting oncogenes, tumor suppressors and interferon (IFN) response genes. We suggest that IDH-mutant gliomas are initially fueled by OPC-like cells in which epigenetic mechanisms activate oncogenic signaling, silence tumor suppressors and suppress IFN responses. The tumors then progress to a more proliferative high-grade malignancy increasingly fueled by NPC-like cells, which lose their hypermethylation and, therefore, become dependent on acquired genetic alterations.

Results

Single-cell accessibility and expression of IDH-mutant gliomas

To investigate regulatory and expression states in IDH-mutant gliomas, we profiled ten tumors by scATAC-seq, including oligodendrogliomas and astrocytomas of different grades (Chromium, 10X Genomics) (Supplementary Table 1 and Extended Data Fig. 1a). We analyzed three of these tumors by scRNA-seq and incorporated published scRNA-seq data for 28 additional tumors[16,17,20–23] into our analyses (Fig. 1a). After applying standard quality control metrics, the scRNA-seq and scATAC-seq datasets included 54,475 and 47,436 cells, respectively (Methods). We clustered and visualized the single-cell data by uniform manifold approximation and projection (UMAP) (Fig. 1a and Extended Data Fig. 1b). We then distinguished malignant cell clusters from stromal and immune clusters on the basis of the expression (or accessibility) of malignant cell-specific (*ASCL1*), immune cell-specific (*CD45* and *CD3D*) and oligodendrocyte-specific (*MOBP*) marker genes. We validated malignant cell assignments on the basis of tumor-specific CNAs (Methods and Extended Data Fig. 1b–d). We focused further analysis on the malignant cell data, including expression profiles for 31,835 single cells and accessibility profiles for 12,156 single cells.

Progenitor cell states and hierarchies in IDH-mutant gliomas

To evaluate the malignant populations, we benchmarked them against published single-cell transcriptomes and accessibility profiles for normal brain cells. Focusing initially on transcriptional data, we clustered and visualized normal cells from three published scRNA-seq datasets for fetal and adult brain[24–26] (2,551 cells; Extended Data Fig. 1e). Evaluation of marker genes across the single-cell clusters confirmed that the UMAP projection captured major cell types, including NPCs, glial progenitor cells (GPCs), OPCs and astrocytes (ACs), as well as mature and immature neurons (Fig. 1b and Extended Data Fig. 1e).

We next projected IDH-mutant malignant cells onto the normal brain scRNA-seq UMAP, positioning each cell according to the principal components derived from the reference brain data (Methods). A majority of malignant cells mapped in the vicinity of normal OPCs, with most remaining cells correlating to NPCs, GPCs or ACs (Fig. 1b and Extended Data Fig. 1f). A small number of malignant cells roughly approximated neurons and expressed marker genes suggestive of immature neurons or differentiating NPCs. We also evaluated the malignant populations using non-negative matrix factorization (NMF), an unbiased method that decomposes single-cell expression data into sets of coordinately regulated genes or 'expression programs'. NMF identified four major programs that were differentially expressed across malignant glioma cells (Fig. 1c). The respective programs were distinguished by the expression of markers for OPCs or GPCs (*APOD*, *PDGFRA*, *OLIG2* and *GFAP*), NPCs or neurons (*SOX4* and *NEUROD1*) and ACs (*APOE* and *ALDH1L1*). Hence, orthogonal analytical approaches identified the same major expression phenotypes among IDH-mutant glioma cells.

Comparison of the two IDH-mutant glioma subtypes (oligodendrogliomas and astrocytomas) revealed that the GPC-like, NPC-like and AC-like states were largely concordant in terms of their expression phenotypes and were represented in both subtypes. In both subtypes, cells that were assigned as GPC-like were intermediate between the OPC-like and NPC-like populations. However, the OPC-like progenitors showed subtle differences (Extended Data Fig. 1g). OPC-like cells in oligodendrogliomas expressed classical OPC markers and programs, while those in astrocytomas also expressed some GPC markers, potentially indicative of broader developmental potential.

We used an analogous strategy to interpret the chromatin accessibility data. We clustered and visualized single cells from published scATAC-seq data for normal brains and inferred the identity of the resultant clusters on the basis of marker gene accessibility (Extended Data Fig. 1e). The accessibility UMAP captured major neural cell types as highlighted in the transcriptomic data, including NPCs, GPCs, OPCs, ACs and mature and immature neurons. We next projected the malignant cell accessibility profiles onto the normal brain UMAP. A majority of malignant cells mapped near OPCs, GPCs or ACs, while a smaller fraction mapped to NPCs or neurons (Fig. 1b). We validated these associations by aggregating malignant cell profiles that projected to a given cluster (pseudobulk) and confirming that OPC-like and AC-like cells had relatively higher accessibility over the promoters of corresponding marker genes (Extended Data Fig. 1h).

Chromatin plasticity of IDH-mutant glioma cells

Our comparative analyses of scATAC-seq and scRNA-seq data were overall concordant in terms of the cellular identities nominated for the major malignant populations. However, the respective data types differed in important ways. When we performed unbiased clustering based on RNA expression of variable genes, the malignant

https://doi.org/10.1038/s43018-024-00865-3

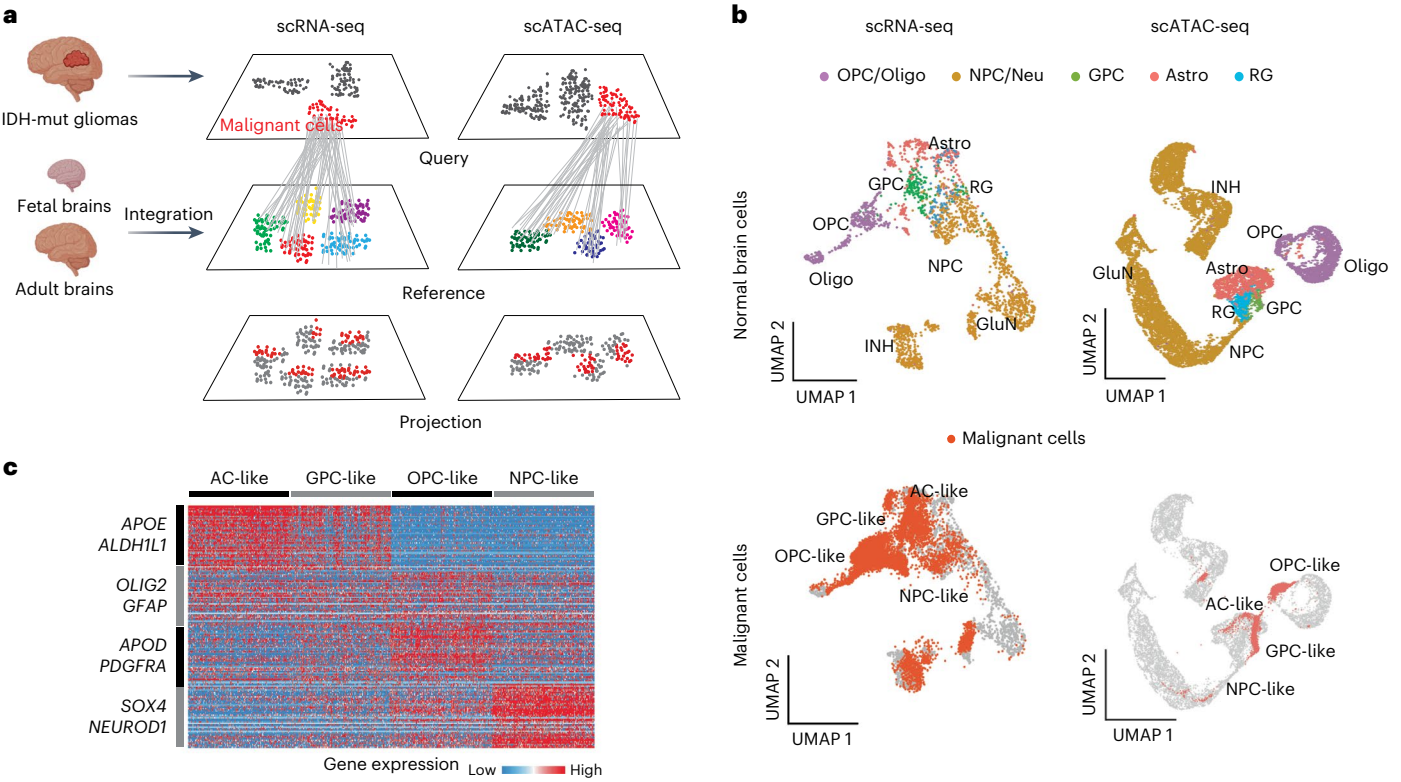

Fig. 1 | scRNA expression and chromatin accessibility in IDH-mutant gliomas. **a**, Schematic depicting the characterization of individual malignant cells by projecting their expression or accessibility profiles onto analogous profiles for fetal and adult brain cells. **b**, Top, UMAP visualizations of scRNA-seq and scATAC-seq data showing clusters of normal neural cells and progenitors (dots) colored by their nominal identities based on marker genes. Abbreviations: RG, radial glial cells; Oligo, oligodendrocytes; INH, inhibitory neurons; GluN, glutamatergic neurons; Neu, neurons; Astro, ACs. Bottom, Malignant IDH-mutant glioma cells (red) from published cohorts (scRNA-seq) and our samples (scATAC-seq) projected onto the same UMAP as above (normal brain cells are gray). **c**, NMF analysis of scRNA-seq data for malignant glioma cells identified four major gene programs. The heat map depicts the expression of genes in each program (rows) across individual malignant cells (columns).

cells segregated into OPC-like, GPC-like, NPC-like and AC-like cells (Fig. 2a, left). This result was qualitatively similar to the supervised projection of the malignant cells onto normal brain cells (Fig. 1b). By contrast, an analogous treatment of the chromatin accessibility data yielded discordant results. Unbiased clustering based on the accessibility of variable peaks (Fig. 2a, right) did not clearly separate the nominal malignant cell types that we had annotated by supervised projection onto the normal brain accessibility map (Fig. 1b).

This observation prompted us to further interrelate the expression and chromatin accessibility profiles of the different malignant cell types. Focusing initially on the scRNA-seq data, we computed cross-correlations among all pairs of cells. We then evaluated the coherence among cells assigned to the same nominal cell type and the divergence between cells assigned to different cell types. Visualization of a cross-correlation map for normal brain cells revealed consistent differences among NPCs, OPCs, GPCs and ACs in terms of their gene expression. A cross-correlation map for malignant cells revealed qualitatively similar differences among NPC-like, OPC-like, GPC-like and AC-like cells (Fig. 2b and Extended Data Fig. 2d).

We next performed an analogous analysis of the scATAC-seq data by computing cross-correlations among all pairs of cells on the basis of the accessibility of differential elements (Methods). Examination of the normal brain data revealed that the respective cell types have distinct chromatin landscapes, consistent with their divergent expression programs. However, examination of the malignant glioma cells revealed that the respective progenitor cell states (OPC-like, GPC-like and NPC-like) were barely distinguishable from one another (Fig. 2b and Extended Data Fig. 2d). To evaluate differences among progenitor cell states more quantitatively, we applied a correlation metric analogous to that previously used to evaluate cellular plasticity in pancreatic cancer[27]. We computed correlations among single cells annotated as the same state and compared the values to correlations among cells annotated as different states. Application of the metric to scATAC data for gliomas confirmed that the different malignant cell states were similar to one another (Fig. 2c). In contrast, an analysis of scATAC data for normal brain cells revealed a clear quantitative distinction (Fig. 2c). This suggests that the different malignant progenitors share a relatively unspecified epigenetic landscape that may be compatible with (or 'permissive of') alternate expression phenotypes.

The notion that different IDH-mutant malignant cell types express distinguishing marker genes and programs without fully specifying their underlying epigenetic state is supported by additional evidence. Inferential analysis of transcription factor (TF) activities based on the accessibility of their cognate motifs revealed similar motif enrichments across the different malignant progenitors (Extended Data Fig. 2a,b). This contrasts with the normal progenitor cell types, whose TF motif enrichments were relatively distinct from one another.

We, therefore, directly compared the respective malignant cell types against their normal counterparts using expression-based and accessibility-based similarity metrics. This revealed that the malignant OPC-like cells were similar to normal OPCs in terms of their transcriptional state and accessibility patterns (Fig. 2d). However, the GPC-like and NPC-like malignant cells did not recapitulate normal GPCs and NPCs (Fig. 2d); rather, their TF motif enrichments were relatively close to those of OPC-like cells (Extended Data Fig. 2b). Hence, while GPC-like and NPC-like malignant progenitors may express GPC and NPC marker

https://doi.org/10.1038/s43018-024-00865-3

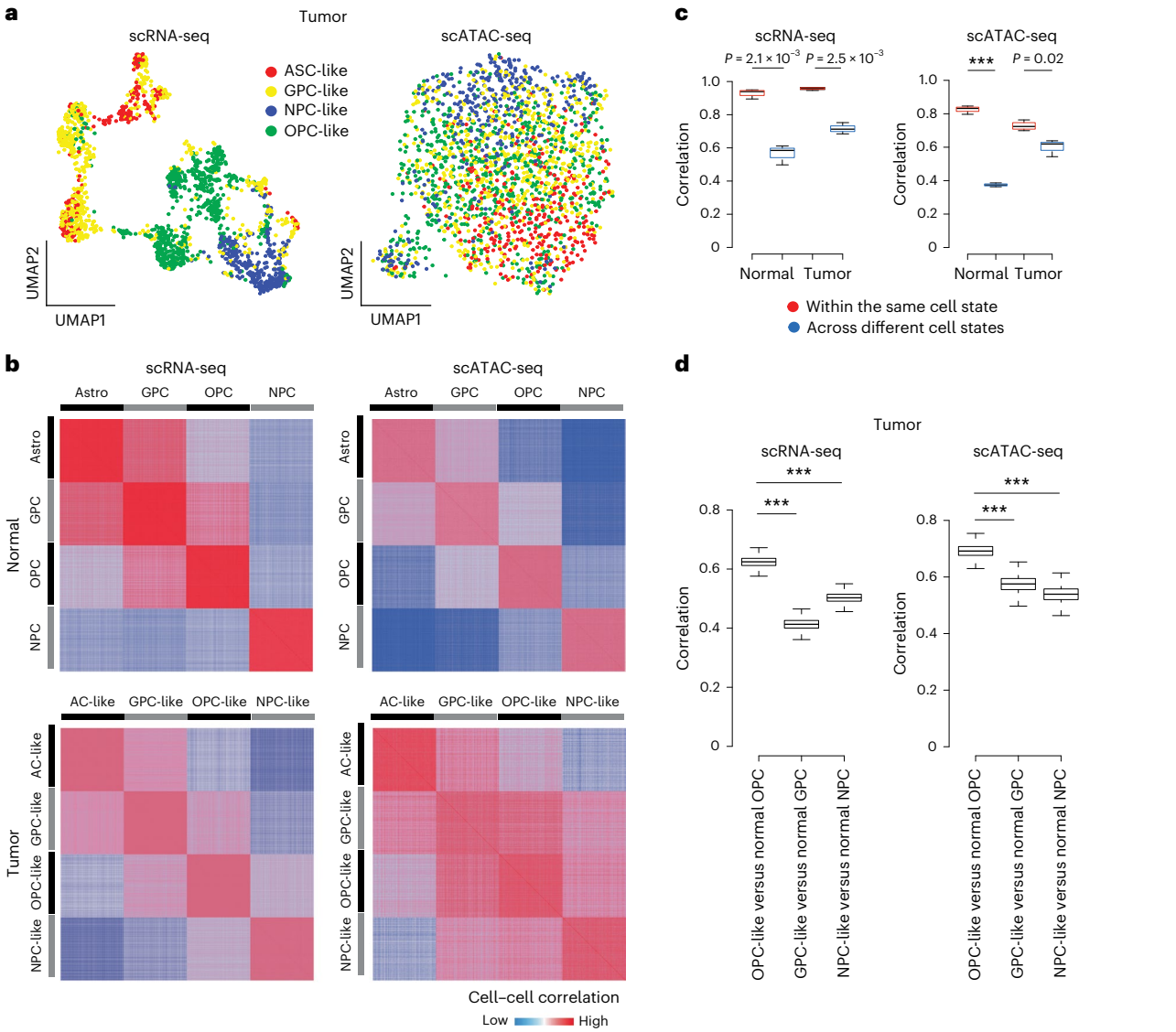

Fig. 2 | Malignant cell types in IDH-mutant gliomas lack chromatin specification. a, UMAP visualization showing the clustering of individual malignant cells based on published scRNA-seq or our scATAC-seq data. Cells are colored by their nominal cell type classification inferred by the projection onto normal brain cell data shown in Fig. 1b. **b**, Top, heat maps showing pairwise correlations of scRNA-seq or scATAC-seq data for normal brain cells (rows and columns) grouped by their cell type classifications. Bottom, heat maps showing pairwise correlations of scRNA-seq or scATAC-seq data for malignant glioma cells (rows and columns) grouped by their cell type classifications. **c**, Box plots show the distribution of correlations between single cells annotated to the same cell state or different cell states in scRNA-seq (each cell state downsampled to $n = 243$ cells) and scATAC-seq data (each cell state downsampled to $n = 133$ cells). Boxes depict the 25th, 50th and 75th percentiles and whiskers depict extreme values. One-tailed t-test P values from left to right: 2.1×10^{-3}, 2.5×10^{-3} and 0.02; $^{***}P < 0.001$. **d**, Box plots showing the distribution of correlations between malignant progenitor cells and corresponding normal progenitors based on scRNA-seq or scATAC-seq data (cell numbers as in **c**). One-tailed t-test P values as in **c**; $^{***}P < 0.001$. Malignant progenitors have relatively concordant accessibility profiles and more closely approximate OPCs.

genes (Fig. 1c and Extended Data Fig. 2a) and gain accessibility over the corresponding promoters (Extended Data Fig. 1h), their global epigenetic landscapes are still closer to OPCs. We also examined OPC-specific enhancers in the *MYC* and *PDGFRA* loci that have been implicated in IDH-mutant gliomagenesis[9,28]. Both elements remained accessible in OPC-like, GPC-like and NPC-like malignant progenitors (Extended Data Fig. 2c). These data are consistent with the hypothesis that IDH-mutant glioma progenitors initially adopt an OPC-like epigenetic state that is permissive to partial reprogramming to GPC-like or NPC-like expression phenotypes.

Glioma progression associated with expansion of NPC-like cells

We next considered how the malignant progenitors change as IDH-mutant gliomas progress from their initial slow-growing stage to a high-grade malignancy. Visualization of single cells in our scRNA-seq UMAP projection suggested that grade 2 tumors are primarily composed of OPC-like, GPC-like and AC-like cells, while grade 3 and 4 tumors are relatively enriched for NPC-like cells (Fig. 3a). To further investigate, we integrated scRNA-seq data for 30 IDH-mutant gliomas ranging from grades 2 to 4, incorporating public datasets[16,17,20–23]. This confirmed that higher-grade tumors have increased proportions of NPC-like cells (Fig. 3b and Extended Data Fig. 3a). During brain development, normal NPCs are more proliferative than OPCs and their other differentiated progeny. Similarly, NPC-like cells appear considerably more proliferative than the other malignant cell types (Extended Data Fig. 3d). To explore this association across a larger clinical cohort, we examined 426 bulk RNA-seq profiles for IDH-mutant gliomas (Supplementary Table 4) from The Cancer Genome Atlas (TCGA)[29]. For each tumor, we estimated

the relative proportions of NPC-like progenitors by comparing signatures of NPC-specific and OPC-specific genes (Methods). Consistent with our scRNA-seq analyses, higher-grade tumors were enriched for NPC-like cells and exhibited a higher expression of proliferation genes (Fig. 3c and Extended Data Fig. 3b).

To evaluate more directly how the relative proportions of NPC-like and OPC-like cells evolve during tumor progression, we compared primary and recurrent IDH-mutant gliomas from the same cohort, using longitudinal data from the GLASS consortium and additional published data[30,31]. Evaluation of bulk RNA-seq data for 19 matched primary and recurrent tumors that progressed from low-grade to high-grade and scRNA-seq for six matched pairs confirmed that the estimated proportions of NPC-like cells were much higher in recurrent tumors (Fig. 3e and Extended Data Fig. 3c). Only a small number of tumors progressed without an increase in the proportions of NPC-like progenitors. These analyses support our overall hypothesis that partial reprogramming of OPC-like progenitors to a proliferative NPC-like phenotype contributes to the progression of IDH-mutant gliomas.

Genetic events associated with NPC expansion and progression

The DNA hypermethylation that is characteristic of IDH-mutant gliomas is frequently lost as these tumors progress to a more aggressive phenotype[15]. Methylation loss is likely because of accelerated replication-associated demethylation in more proliferative tumor cells. Indeed, when we ordered TCGA tumors by their proliferation scores, we confirmed that the most proliferative NPC-enriched tumors were relatively depleted of methylation (Fig. 3d). This suggests that proliferative NPC-like malignant progenitors have lower DNA methylation and may, thus, lose methylation-dependent oncogenic drivers.

Previous work by us and others suggests that DNA hypermethylation drives gliomagenesis by disrupting insulation, thereby inducing the *PDGFRA* proto-oncogene, and by silencing the *CDKN2A* tumor suppressor locus[8–11]. These epigenetic effects should decline as glioma progenitors lose hypermethylation. We, therefore, investigated whether proliferative NPC-enriched tumors acquire genetic alterations that could compensate for the loss of methylation-dependent drivers. Indeed, these advanced tumors were enriched for amplifications involving the *PDGFRA*, *MYCN* and *CDK4* oncogenes and for deletions of *CDKN2A* and other tumor suppressor loci (Fig. 3d and Supplementary Table 2). These events could readily compensate for the loss of epigenetic oncogene activation and tumor suppressor silencing in proliferative NPC-like cells.

We extended this analysis through an in-depth characterization of a single IDH-mutant astrocytoma for which we generated scRNA-seq data for multiple regions of the tumor. We identified three major subclones in this tumor on the basis of inferred CNAs, which included *CCDN2* and *MYCN* amplifications and *CDKN2A* deletion (Methods). Integration of cell states and CNA information enabled us to infer a putative phylogeny in which this tumor first acquired *CCND2* amplification (subclone 1), followed by *CDKN2A* deletion (subclone 2) and finally *MYCN* amplification (subclone 3). Each single-cell profile could be assigned to one of these subclones on the basis of inferred copy number variations (CNVs). Subclone 3, which harbored all three genetic alterations, was highly enriched for NPC-like cells with a high expression of proliferation genes (Fig. 3g,h). A similar analysis of a second tumor[32] with multiple genetic subclones also revealed the enrichment of NPC-like cells in the more advanced subclone (Extended Data Fig. 3f).

We also leveraged bulk RNA-seq data for longitudinal specimens to evaluate these specific CNAs in matched primary and recurrent tumors[30]. This confirmed that CNAs involving *PDGFRA*, *CCDN2* and *MYCN* amplification or *CDKN2A* deletion occur at a much higher frequency in high-grade recurrent tumors than in the prior low-grade resections from the same cohort (Fig. 3f). These collective analyses are consistent with the hypothesis that, while OPC-like cells in low-grade IDH-mutant gliomas may be largely sustained by epigenetic alterations, the more proliferative progenitors in advanced tumors become increasingly dependent on genetic drivers as their hypermethylation is lost.

Suppression of IFN responses in IDH-mutant gliomas

Another striking outcome of these genetic analyses was that NPC-enriched tumors harbor multiple deletions of immune genes implicated in IFN responses (Fig. 3d). These include a large *IFNA* and *IFNB* (*IFNA/B*) gene cluster on chr9 that is recurrently lost in conjunction with the adjacent *CDKN2A* tumor suppressor locus. The pattern and frequency with which the *IFNA/B* cluster is lost across many tumor types indicates that it confers fitness independently of *CDKN2A* (ref. 33). Remarkably, *IFNA/B* deletion was more prevalent in gliomas than other tumor types and, moreover, was strongly biased toward NPC-enriched grade 4 tumors ($P < 2.2 \times 10^{-16}$; Supplementary Table 3 and Fig. 3d).

In addition to the *IFNA/B* cluster, high-grade IDH-mutant gliomas were enriched for chromosomal deletions involving *IFIT1*, *STAT1*, *IRF1* and *SETD2* ($P < 2.2 \times 10^{-16}$; Fig. 3d and Supplementary Table 2). *IFIT1*, *STAT1* and *IRF1* encode direct mediators of IFN responses, while *SETD2* encodes a methyltransferase whose disruption in melanoma and other solid tumors has been shown to suppress IFN signaling[34]. IFN responses in cancer cells can cause cell-cycle arrest and drive both innate and adaptive immunity. Our analyses indicate that suppression of IFN responses confers a fitness advantage to IDH-mutant gliomas.

These genetic findings also raise the question of whether and how early OPC-enriched IDH-mutant gliomas evade IFN responses. We considered two possibilities: OPC-like progenitors might be relatively insensitive to IFN signaling or, alternatively, their DNA hypermethylation might suffice to suppress the pathway. To investigate, we compared grade 2 IDH-mutant oligodendrogliomas ($n = 81$) to a cohort of grade 2 IDH-WT gliomas ($n = 19$) from TCGA (Fig. 4a and Extended Data

Fig. 3 | Cell states and genetic alterations associated with glioma progression. a, Malignant cells projected onto scRNA-seq UMAP for normal brain as in Fig. 1b but with malignant cells colored by tumor grade. **b**, Box plots depict estimated proportions of OPC-like and NPC-like cells in scRNA-seq data ($n = 30$) for tumors stratified by grade ($n = 12$ for grade 2, $n = 13$ for grade 3 and $n = 5$ for grade 4). Boxes depict the 25th, 50th and 75th percentiles and whiskers depict extreme values. One-tailed *t*-test *P* values from left to right: 0.04 and 0.015. **c**, Box plots depicting relative proportions of NPC-like versus OPC-like cells (left) or proliferation scores (right), inferred from TCGA RNA-seq for IDH-mutant gliomas ($n = 426$) stratified by grade ($n = 195$ for grade 2, $n = 174$ for grade 3 and $n = 7$ for grade 4). One-tailed *t*-test *P* values from left to right: 0.028, 2.1×10^{-3} and 0.011; $^{***}P < 0.001$. **d**, IDH-mutant gliomas (columns) ordered by proliferation scores ($n = 417$). Top rows depict tumor grade, global DNA methylation and relative proportions of NPC-like versus OPC-like cells. Additional rows depict copy number gains (red) and losses (blue) for variable cytobands with indicated genes. **e**, Line plot depicting relative proportions of NPC-like versus OPC-like cells, inferred from bulk RNA-seq for matched primary and recurrent IDH-mutant gliomas ($n = 19$)[30]. Thin gray lines connect data points for the same participant, while the red line and shaded area depict the imputed average and confidence interval. **f**, Heat maps showing focal copy number gains (red) and losses (blue) for indicated gene loci in primary (P) and recurrent (R) IDH-mutant gliomas (each row corresponds to one of 64 participants)[30]. Heat ranges from +2 (likely high-level amplification) to −2 (likely homozygous deletion), while intermediate values predict likely amplification (+1), deletion (−1) or copy neutral (0)[70]. **g**, Plot depicting CNAs for loci containing *CCND2*, *CDKN2A* and *IFNA/B* clusters or *MYCN* (rows) across 2,350 cells (columns) from one IDH-mutant glioma. Malignant cells are grouped into three subclones on the basis of CNAs and compared to normal cells from the same resection (left). Malignant cell state assignments are indicated. **h**, Subclonal hierarchy reconstructed from CNAs in single cells: *CCND2* amplification is followed by *CDKN2A* and *IFNA/B* deletion and then *MYCN* amplification. Initial clones comprise OPC-like cells (blue), while the late-arising clone is enriched for NPC-like cells (yellow). Glioma progression is associated with the expansion of proliferative NPC-like cells with characteristic CNAs.

https://doi.org/10.1038/s43018-024-00865-3

Fig. 4a). Both cohorts exhibited similarly low proliferation signatures per RNA-seq, consistent with their histology (Extended Data Fig. 4b). As expected, global methylation levels were substantially higher in the IDH-mutant tumors (Extended Data Fig. 4b and Fig. 4a). Notably, the IDH-mutant cohort had significantly lower IFN scores ($P < 2.2 \times 10^{-16}$), consistent with the possibility that hypermethylation subdues IFN responses (Fig. 4a,b and Extended Data Fig. 4a,b). These data suggest that OPC-like and NPC-like malignant progenitors both evade IFN signaling but do so through distinct strategies predicated on epigenetic or genetic mechanisms, respectively.

DNMT1 inhibition activates IFN signaling in glioma models

To test the impact of DNA methylation on IFN signaling directly, we established short-term organoid cultures from a low-grade IDH-mutant

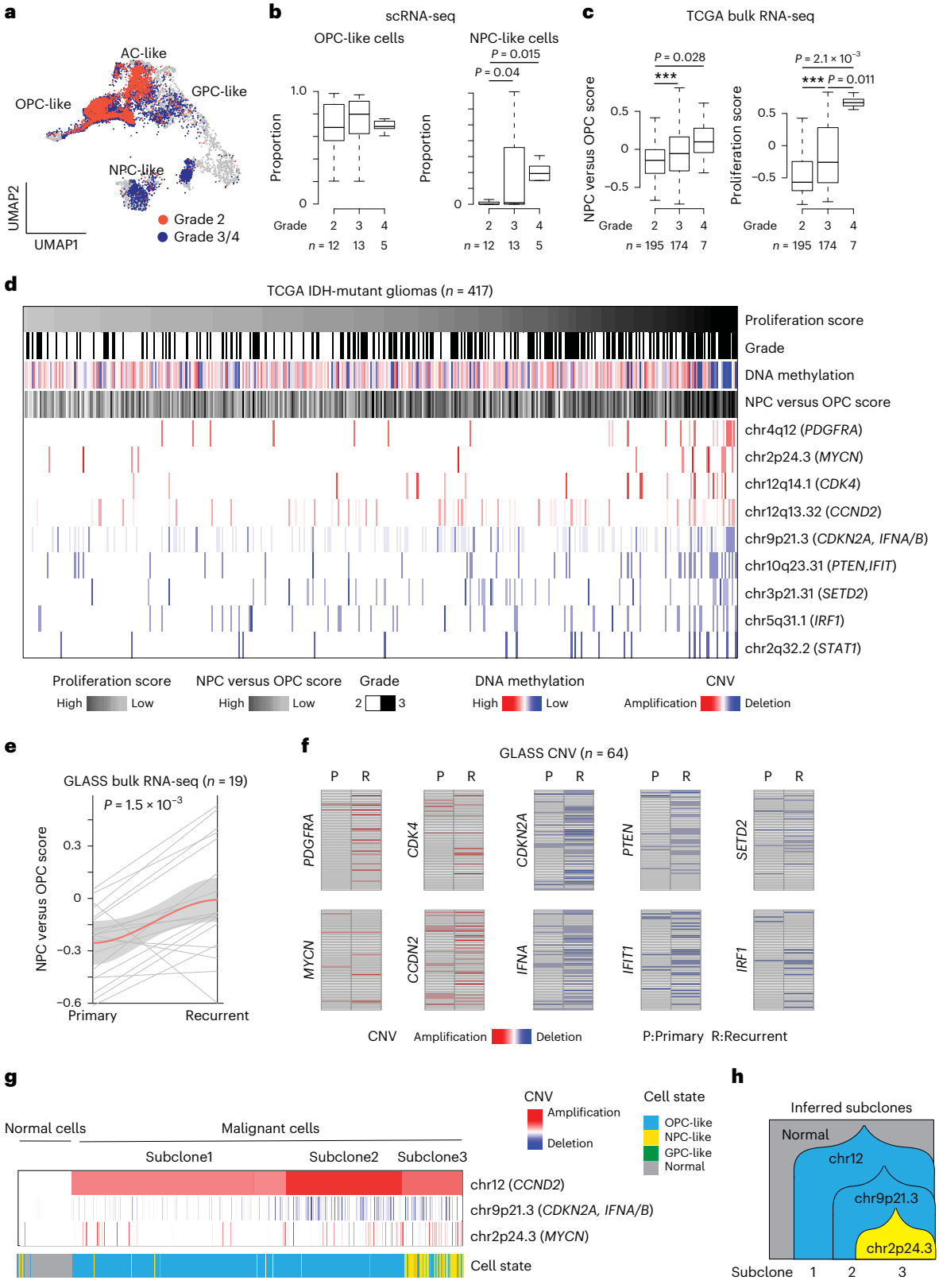

https://doi.org/10.1038/s43018-024-00865-3

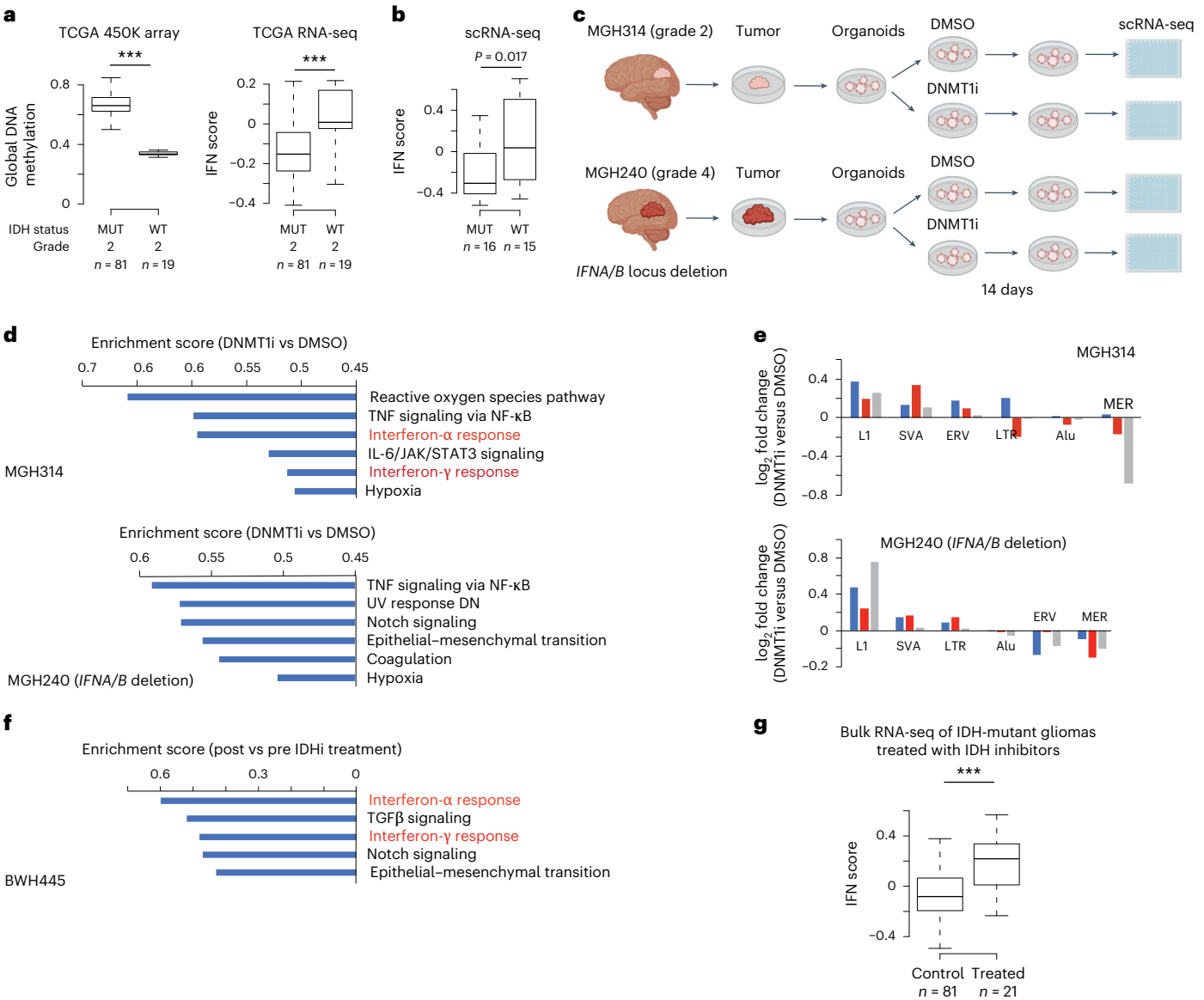

Fig. 4 | Suppression of IFN responses in IDH-mutant gliomas. a, Box plots depicting global DNA methylation levels (450K array) and IFN signature scores (RNA-seq) for grade 2 IDH-mutant oligodendrogliomas ($n = 81$) and grade 2 IDH-WT gliomas ($n = 19$) from TCGA (per 2016 WHO classification). Boxes depict the 25th, 50th and 75th percentiles and whiskers depict extreme values. One-tailed *t*-test *P* values: ***$P < 0.001$. **b**, Box plot depicting IFN scores for malignant cells in scRNA-seq data for IDH-mutant[16,17] ($n = 16$ specimens) and IDH-WT gliomas[71] ($n = 15$ specimens). One-tailed *t*-test *P* value: 0.017. **c**, Schematic depicting two IDH-mutant glioma organoids treated with DNMT1 inhibitors and profiled by scRNA-seq. The MGH314 organoid was prepared from a grade 2 tumor with an intact *IFNA/B* cluster, while the MGH240 organoid was prepared from a grade 4 tumor with *IFNA/B* cluster deletion. **d**, Bars depicting enrichment scores for gene sets upregulated by DNMT1 inhibitors per GSEA. **e**, Plots showing the relative change in transposable element expression upon DNMT1 inhibitor treatment per scRNA-seq. Colors indicate three technical replicates. **f**, Bars depicting enrichment scores for gene sets upregulated in an IDH-mutant glioma resected from a person treated with an IDH inhibitor per scRNA-seq, relative to pretreatment control. **g**, Box plots depicting IFN signature scores (RNA-seq) for IDH-mutant oligodendrogliomas (grade 2, $n = 21$ specimens) resected from persons treated with an IDH inhibitor compared to control oligodendrogliomas (grade 2, $n = 81$, specimens) from TCGA. One-tailed *t*-test *P* values: ***$P < 0.001$. These analyses suggest that mutations in IDH genes and DNA hypermethylation suppress IFN responses in low-grade gliomas.

glioma (MGH314) and a high-grade IDH-mutant glioma with IFN locus deletion (MGH240)[35,36]. The single-cell transcriptomic analysis confirmed that the organoids recapitulate key aspects of the primary tumor, including the presence of varying proportions of OPC-like, NPC-like and AC-like malignant cells with faithful expression phenotypes (Extended Data Fig. 4d,e). We treated both models with a DNA methyltransferase 1 (DNMT1) inhibitor (GSK-3484862) to reduce global DNA methylation and evaluated transcriptional changes by scRNA-seq (Fig. 4c). The demethylating agent led to robust upregulation of methylation-sensitive genes and IFN pathway genes (Fig. 4d, Supplementary Table 5 and Extended Data Fig. 5a,b). The changes were most pronounced in the grade 2 model, consistent with a critical role for methylation in suppressing IFN programs (Fig. 4d and Extended Data Fig. 5b). We also detected upregulation of transposable elements, including the LINE1 family, which is implicated in the production of RNA–DNA hybrids capable of activating the cyclic GMP–AMP synthase (cGAS)–stimulator of interferon genes (STING) pathway and downstream IFN signaling[37] (Fig. 4e).

We next explored whether emerging clinical data could provide insight into our study and findings. A recent clinical study showed that a small-molecule inhibitor of the mutant IDH enzyme prolonged progression-free survival in participants with grade 2 IDH-mutant

gliomas[38]. RNA-seq data for tumors in a surgical window-of-opportunity study evaluating this inhibitor revealed that inhibitor treatment was associated with a shift toward more differentiated cell states, consistent with progenitor differentiation[39,40]. The study noted upregulation of IFN pathway genes in a subset of participants but did not distinguish whether this reflected malignant cell changes or increased immune infiltration[39]. However, reanalysis of these data using our malignant cell-specific IFN signature suggested that IDH inhibitor treatment increases IFN signaling in the malignant glioma cells (Fig. 4g and Extended Data Fig. 4c). We also examined scRNA-seq data for three additional gliomas from persons treated with IDH inhibitors[40]. Unbiased analysis of these data identified an IFN signaling program as a top upregulated gene set in malignant cells from the treated tumors (Fig. 4f and Extended Data Fig. 5d). The cells also exhibited gene markers of methylation loss, consistent with the expected mechanism of the IDH inhibitors (Extended Data Fig. 5c). Together, these bulk and single-cell analyses suggest that IDH inhibition can reduce DNA methylation levels and induce an IFN response in lower-grade IDH-mutant gliomas, with a potential impact on progenitor differentiation. They provide strong in vivo support for our hypothesis that DNA hypermethylation suppresses IFN responses in these tumors.

Lastly, we examined the impact of demethylation on cell type distributions in the glioma organoids. DNMT1 inhibition led to a proportional increase in the number of AC-like cells in the IDH-mutant models (Fig. 5a). A similar shift toward AC-like cells was evident in tumors from persons treated with IDH inhibitors[40]. This differentiation could be a consequence of the increased IFN signaling, at least in part, as prior studies have shown that inflammatory cytokines such as tumor necrosis factor induce AC differentiation[41]. Moreover, normal brain ACs tolerate higher IFN activity than progenitor cells[42]. This phenomenon appears to be recapitulated in gliomas as our scRNA-seq data confirm that AC-like cells have higher IFN signatures than the malignant progenitors (Fig. 5b). This difference is also evident at the level of chromatin accessibility in that IFN-regulatory factor (IRF)–signal transducer and activator of transcription (STAT) motif enrichments in the scATAC-seq data were most pronounced for the AC-like population (Fig. 5c). Given that higher proportions of NPC-like cells are associated with reduced overall survival (Fig. 5d and Extended Data Fig. 5e), these data suggest the potential of demethylating agents and IDH inhibitors to activate an IFN response and slow the progression of IDH-mutant gliomas, particularly in tumors that have yet to acquire genetic CNAs of IFN-related gene loci.

Taken together, our data support a model in which DNA hypermethylation confers fitness to OPC-like cells that fuel early tumorigenesis by silencing tumor suppressors, suppressing IFN responses and inducing oncogene expression. As IDH-mutant gliomas progress, a population of cells with NPC-like transcriptional programs expands, potentially through partial reprogramming of OPC-like cells. As the proliferative NPC-like cells lose their global hypermethylation, they acquire genetic CNAs that drive the aggressive and ultimately lethal phenotypes of high-grade IDH-mutant gliomas.

Discussion

Our single-cell study of the heterogeneous epigenetic cell states, transcriptional programs and genetic alterations in IDH-mutant gliomas uncovers biological insights and presents a mechanistic model of progression with implications for diagnosis and treatment. In particular, we identify epigenetic plasticity of glioma progenitor states, interplay between epigenetic and genetic tumor drivers and alternate mechanisms of IFN suppression as critical for the progression of these tumors.

First, we examined the gene-regulatory circuits and plasticity of glioma cells by comparing their single-cell chromatin accessibility and gene expression to normal fetal and adult neural cell types. Malignant glioma cells enact gene expression programs reminiscent of OPCs, GPCs, NPCs or ACs. Yet despite their transcriptional differences, OPC-like, GPC-like and NPC-like malignant cells share similar chromatin landscapes and do not appear to specify in terms of their epigenetic regulation. In fact, our analysis suggests that most glioma progenitors exhibit accessibility profiles and TF motif enrichments largely consistent with an OPC-like state.

These results raise the question of how cells with an OPC-like chromatin state can enact such a broad spectrum of transcriptional programs, including the expression of NPC gene signatures and markers. A clue comes from our observation that the alternate malignant cell states change in proportion as gliomas progress. Low-grade IDH-mutant tumors are composed primarily of OPC-like and AC-like cells, presumably fueled by the former, where cell-cycle activity is confined[17]. High-grade IDH-mutant tumors are relatively enriched for NPC-like cells whose increased proliferation rates coincide with an aggressive clinical phenotype. Although these NPC-like cells exhibit distinguishing transcriptional programs and surface phenotypes[16,17], their epigenetic landscapes and core regulatory circuits do not notably diverge from the originating OPC-like cells. We suggest that IDH-mutant glioma initiation involves the transformation of OPCs to OPC-like malignant cells whose acquisition of epigenetic plasticity facilitates a partial reprogramming of their expression state to a proliferative NPC-like phenotype (Extended Data Fig. 3e). We note that contemporary studies provide orthogonal support for the hypothesis that OPCs represent a cell of origin for IDH-mutant gliomas. We and others have established causal roles for the OPC marker gene *PDGFRA* and a nearby OPC-specific enhancer in gliomagenesis[9,43–45]. A genetic variant in the *MYC* locus that is associated with IDH-mutant glioma risk[28] also coincides with an OPC-specific enhancer. Lastly, a recent study of normal human brains detected clonal *IDH1* mutations in glial fractions enriched for OPCs, consistent with a fitness role for mutant IDH in OPCs[46]. A scenario in which IDH-mutant gliomas initiate as OPC-like progenitors that subsequently transition to a more aggressive NPC-like state may help explain how a single stereotyped transformation event can yield such heterogeneous malignant cell states and tumor phenotypes (Fig. 5e and Extended Data Fig. 3e).

Second, our analyses suggest that tumor progression is associated with a switch from epigenetic to genetic drivers (Fig. 5e). IDH-mutant tumors produce high levels of the oncometabolite D-2HG, which inhibits DNA demethylases, causing their characteristic hypermethylation. We and others have shown that DNA hypermethylation induces the proto-oncogene *PDGFRA* by unleashing a nearby OPC-specific enhancer and silences the tumor suppressor locus *CDKN2A* (refs. 9,47,48). Although methylation-dependent drivers may sustain indolent OPC-like progenitors in low-grade IDH-mutant tumors, hypermethylation is lost upon tumor progression[15], presumably because of passive methylation loss in the proliferative progenitors. Consistently, high-grade tumors acquire additional genetic alterations, including *CDKN2A* locus deletion and amplifications of *PDGFRA* and other oncogenes, which enable NPC-like cells to drive progression. This recognition that IDH-mutant gliomas of different stages are driven by distinct molecular mechanisms is consistent with clinical observations and has important therapeutic implications[2]. Progressed or relapsed tumors with characteristic genetic alterations will be less likely to respond to interventions that target mutant IDH or associated methylation changes.

Third, we find that IDH-mutant gliomagenesis is dependent on the suppression of IFN responses. The underlying mechanisms again vary by grade, with low-grade gliomas reliant on the suppressive impact of methylation[49,50] and high-grade gliomas reliant on genetic lesions. The latter include deletions of the *IFNA/B* cluster, *IRF1*, *STAT1* and the chromatin regulator gene *SETD2*, which has established roles in IFN signaling. The observation that the genetic alterations are relatively specific to NPC-enriched, high-grade tumors implies that low-grade tumors must either tolerate IFN responses or suppress them by other mechanisms. In support of the latter, we find that IFN expression

https://doi.org/10.1038/s43018-024-00865-3

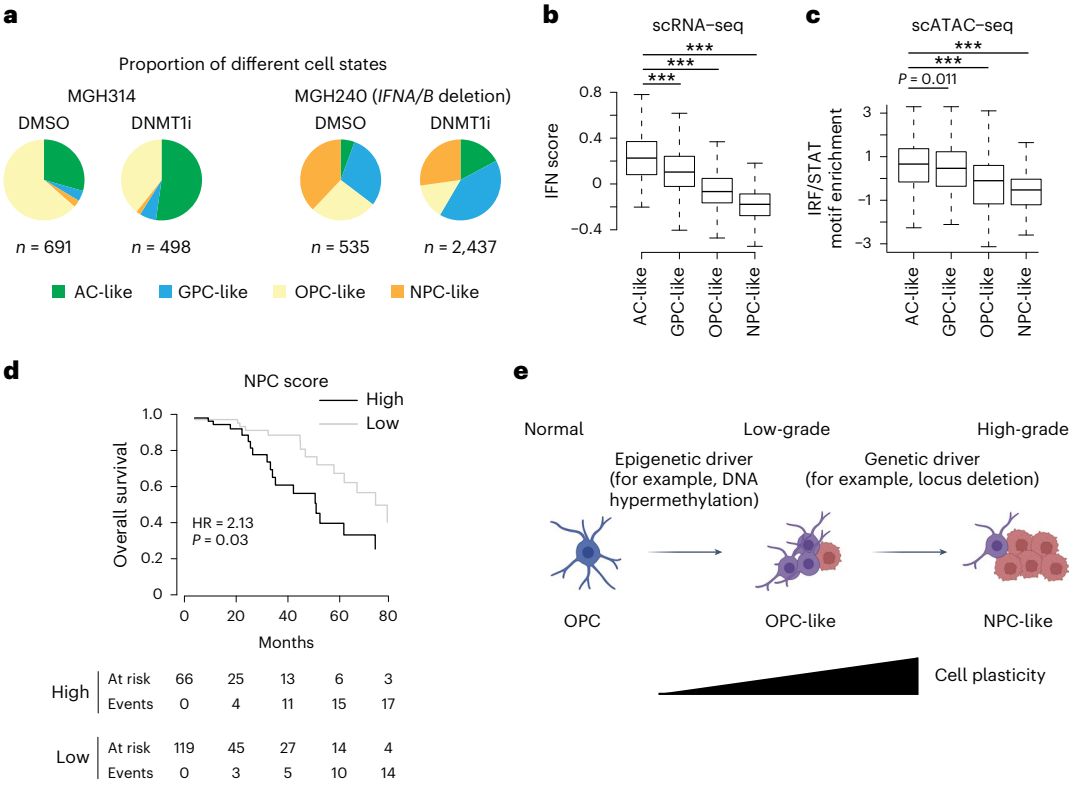

Fig. 5 | Malignant cell states are associated with different IFN levels and patient outcomes. a, Pie charts showing the distribution of malignant cell states, assigned by scRNA-seq, in patient-derived organoids treated with DNMT1 inhibitor or control. **b**, Box plots depict IFN signature scores across individual malignant cells stratified by their assigned states (243 AC-like cells, 1,113 GPC-like cells, 7,378 OPC-like cells and 311 NPC-like cells). Boxes depict the 25th, 50th and 75th percentiles and whiskers depict extreme values. One-tailed *t*-test *P* values: ***$P < 0.001$. **c**, Box plots depicting the enrichment of IRF–STAT motif accessibility across individual malignant cells stratified by assigned cell state (each state downsampled to $n = 100$ cells). One-tailed *t*-test *P* values: 0.011 between AC-like and GPC-like; ***$P < 0.001$. **d**, Kaplan–Meier curves for high-grade (grades 3 and 4) IDH-mutant gliomas ($n = 185$), stratified by NPC enrichment score. Hazard ratios (HRs) and *P* values associated with NPC-enriched tumors are indicated. **e**, Schematized model proposing that IDH-mutant gliomas initiate through the transformation of OPC cells (blue) to slow-growing OPC-like malignant cells (purple) driven by epigenetic changes involving DNA hypermethylation. During tumor progression, OPC-like cells partially reprogram to proliferative NPC-like cells (red) that lose their hypermethylation and become dependent on genetic drivers.

signatures are low in hypermethylated low-grade IDH-mutant gliomas, relative to low-grade IDH-WT gliomas. Suppression may be mediated by methylation-dependent silencing of transposable elements[51], STING and/or the IFN-related genes themselves[52]. Alternatively or additionally, it could involve direct effects on cGAS–STING reactivity[53,54].

NPCs are highly sensitive to IFN, which drives differentiation and/or cell death[41]. Our data suggest that malignant glioma progenitors are similarly sensitive to innate IFN responses, which may drive their differentiation and/or apoptosis. These responses may be cell autonomous or may be augmented by IFN released into the tumor microenvironment by myeloid cells or T cells. Either way, the malignant progenitors appear to be under strong selection to evade these responses, initially through hypermethylation and subsequently through the various genetic deletions associated with NPC-enriched, high-grade IDH-mutant gliomas.

We also recognize caveats to our data and conclusions. Our chromatin accessibility profiles were relatively limited in terms of participant numbers. Although we sought to augment all conclusions with scRNA-seq and bulk expression profiles for much larger cohorts, characterization of additional tumors by scATAC-seq or other epigenetic assays may implicate additional mechanisms and loci or otherwise refine our proposed progression model. Furthermore, our conclusions on the temporal order of events in tumorigenesis are inferential. We propose the transformation of an OPC cell of origin to an OPC-like malignant progenitor as an initiating step that is followed by partial reprogramming to an NPC-like state during tumor progression. However, our analysis of paired primary and recurrent tumors suggests that a small number of progressed tumors are driven by progenitors that retain an OPC-like phenotype. Moreover, we cannot rule out the possibility that a subset of tumors initiate as NPC-like progenitors, a scenario that would also be consistent with prior single-cell studies[16] and with prior reports that introduction of mutant IDH into ACs or gliomasphere cultures reprograms their epigenomes toward an NPC-like state[55]. That being said, the rarity of NPC-like progenitors in low-grade tumors, the OPC-like character of their epigenetic states and our related findings lead us to favor an OPC-centric model of initiation.

In conclusion, we present single-cell accessibility and expression profiles for malignant cells within IDH-mutant gliomas at successive stages of clinical progression. Integration of these and complementary datasets leads us to a model in which IDH-mutant gliomas are initially fueled by indolent OPC-like progenitors that are sustained in large part by methylation-dependent activation of oncogenic signaling, *CDKN2A* silencing and suppression of IFN responses. The initiating progenitors have inherent plasticity that facilitates their partial reprogramming to an NPC-like phenotype that underlies tumor progression. The relatively higher proliferation rates of the NPC-like progenitors cause them to lose their methylation-dependent epigenetic drivers, which in turn creates intense selection pressure for the acquisition of genetic alterations that activate oncogenic signaling, inactivate *CDKN2A* and disrupt IFN signaling. The acquired genetic lesions underpin an aggressive and ultimately fatal tumorigenesis and likely constrain the efficacy of epigenetic therapies.

Methods

Tumor acquisition and single-cell sorting

All subjects gave their informed consent before their tumor samples were obtained for study. There was no selection for race, ethnicity or other socially relevant groupings. Demographic information on the subjects is provided in Supplementary Table 1. The protocol was approved by the Institutional Review Board of the Dana-Farber and Harvard Cancer Center (protocol #10-471). Subjects did not receive compensation. Tumor samples were collected from the pathology laboratory shortly after surgical resection. The presence of a mutation in IDH genes was predicted on the basis of age and radiographic tumor appearance and subsequently confirmed by clinical immunohistochemistry and next-generation sequencing assays. Fresh tumor samples were dissociated using a papain-based brain tumor dissociation kit (Miltenyi Biotec) and processed for single-cell analysis as previously described[17]. Briefly, cells were blocked and stained with CD45–VioBlue direct antibody conjugate (Miltenyi Biotec, 130-113-122), washed with cold PBS and then resuspended in 1 ml of BSA and Hank's balanced salt solution with 1 mM calcein AM (Thermo Fisher Scientific, C1430) and 0.33 mM TO-PRO-3 iodide (Thermo Fisher Scientific, T3605) for 30 min. Sorting was performed on an FACS Aria Fusion (Becton Dickinson) using 488-nm (calcein AM, 530/30 filter), 640-nm (TO-PRO-3, 670/14 filter) and 40-nm (CD45–VioBlue, 450/50 filter) lasers. Doublets and gate-only singleton cells were discriminated by strict forward scatter height versus area criteria. We sorted individual viable (positive for calcein AM and negative for TO-PRO-3) immune and nonimmune single cells into 1.5-ml Eppendorf tubes with PBS and 1% BSA. After the sorting, we immediately proceeded to the scRNA-seq and scATAC-seq experiments.

scRNA-seq and scATAC-seq experiments

scRNA-seq was performed using Seq-Well as previously described[56], applying 12,000 cells to the arrays, performing 18 PCR cycles for whole-transcriptome amplification and using a template-switching oligo with a locked nucleic acid modification of the last nucleotide. Sequencing libraries were prepared using Nextera reagents (Illumina, FC-131-1096) and sequenced on an Illumina NextSeq 500. The read lengths were 20 cycles for read 1, 8 cycles for the library index and 50 or 64 cycles for read 2.

scATAC-seq was performed using the 10X Genomics platform as previously described[57]. Briefly, nuclei were prepared, pelleted, resuspended in lysis buffer, washed with 200–400 µl of wash buffer and counted with trypan blue. They were resuspended in nuclei buffer such that there were ~2,000 nuclei per µl. For tagmentation, 5 µl of this suspension was combined with 7 µl of ATAC buffer (10X Genomics) and 3 µl of Tn5 and incubated at 37 °C for 1 h. Libraries were prepared per the 10X Genomics scATAC-seq protocol and sequenced on an Illumina NextSeq 500.

Generation of patient-derived IDH-mutant glioma organoid and DNMT1 inhibitor treatment

IDH-mutant glioma organoids were established and cultured as previously described[35]. Briefly, primary tumor pieces from the operating room were distributed in six-well culture plates with 4 ml of organoid medium and placed on an orbital shaker rotating at 120 rpm in an incubator (37 °C, 5% CO_2 and 90% humidity). The medium was changed every other day without disturbing the organoid by tilting the plates. Tumor pieces generally formed rounded organoids within 2 weeks. After 2–3 weeks of maturation of the organoids, 4 µl of DNMT1 inhibitor (GSK-3484862)[58] or DMSO were added to the medium to a final concentration of 1 µM. The medium was changed every other day with new DNMT1 inhibitor added to the same concentration. Treatment was continued for 14 days until the samples were isolated for Seq-Well scRNA-seq experiments.

Processing of scRNA-seq data

For scRNA-seq performed using Seq-Well, FASTQ files were aligned to GRCh38 with STARsolo[59] using the following parameters: '--soloType CB_UMI_Simple --soloCBstart 1 --soloCBlen 12 --soloUMIstart 13 --soloUMIlen 8 --outSAMtype BAM SortedByCoordinate --outSAMattributes CR UR CY UY CB UB'. The resulting raw matrices were gzipped and used as input for Seurat through the Read10X() function with default parameters. Gene module scores were calculated using the Seurat AddModuleScore function. Malignant cells were identified by calculating the usage values of glioma expression programs. We uploaded a normalized gene expression matrix using the 'annotation mode' in the glioma program calculator[32]. For a cell to be annotated as malignant, the cell had to have the highest usage for one of the malignant glioma programs and less than 20% usage for any other nonmalignant expression program. For scRNA-seq in published cohorts, we used the malignant cell identification from the literature and validated by gene expression.

Processing of scATAC-seq data

CellRanger ATAC (version 1.1.0) was used for alignment, deduplication and generation of the single-cell matrix, using GRCh38 as a reference. Cells with more than 30,000 reads or fewer than 3,000 reads were excluded from the analysis. Quality control was performed using Signac with the following parameters: 'pct_reads_in_peaks > 15, blacklist_ratio < 0.05, nucleosome_signal < 4 and TSS.enrichment > 3'. Custom scripts were used to estimate copy number variants. cisTopic[60] and Signac[61] were used to cluster all cells for the identification of cluster-specific peaks and UMAP visualization. Gene activity scores were calculated by Signac. We used shared nearest neighbor clustering to distinguish malignant cell clusters with gene activity scores from several specific gene categories: genes specific to malignancy (*EGFR*, *ASCL1*, *PDGFRA* and *DCX*), genes unique to normal oligodendrocytes (*MBP* and *MOBP*), genes specific to myeloid cells (*PTPRC*) and genes unique to T cells (*CD3D* and *CD3E*). This approach enabled us to accurately identify clusters of malignant cells. To refine our analysis and reduce the inclusion of potential doublets, we excluded malignant cells exhibiting high gene activity scores (greater than 1) for markers associated with nonmalignant cells. We validated these assignments using CNVs for individual tumors. We conducted CNV analysis using two distinct methods. First, we generated a gene activity matrix using Signac, which was then used as input for inferCNV[16]. Second, we produced a genome-wide bin-based count matrix with the FeatureMatrix function of Signac. The matrix was normalized by subtracting the 0.2 or 0.8 percentile values of the normal cell types to reflect deviations from a baseline established by the normal cell type distribution.

Reference projections

Projections of the scRNA-seq and scATAC-seq malignant cells onto the normal brain cells was performed using Seurat[62]. Published fetal and adult data from scRNA-seq[24–26] and scATAC[24,25] were integrated into the normal brain cell reference map and cell types were annotated on the basis of the original reports. For scRNA-seq data, variable genes for principal component analysis (PCA) were selected on the basis of the normal brain cell data. Transfer anchors were identified using PCA reduction. For scATAC-seq data, all malignant cell fragments were quantified on the peak feature of normal brain cells. Transfer anchors were identified using latent semantic indexing reduction. Cell states were assigned on the basis of the maximum prediction score for each lineage.

NMF analysis

We performed NMF analysis using the consensus NMF (cNMF) package[63]. Briefly, we identified the top 2,000 variable genes in the oligodendroglioma and astrocytoma Smart-seq2 scRNA-seq datasets[16,17] using Seurat's 'FindVariableFeatures()' function. In addition to these variable genes, we included genes defined as markers for stemness, oligocyte and AC lineages[16]. We filtered the gene expression matrix to include only these variable genes and marker genes. In the 'prepare' script of cNMF, we set '-n-iter' to 200 and tested over *K* values ranging from 2 to

25. We then performed factorization ('factorize'), combination and *K* plot generation ('k_selection_plot') scripts. We selected $K = 7$ from the K plot because of the high stability and low error rate at this value. We ran the 'consensus' script with '--local-density-threshold' set to 0.025 and '--components' set to 7. This script generated the usage matrix and the gene spectra.

Differential motif enrichment analysis

Motif enrichment scores for scATAC-seq data of glioma cells and normal brain cells were identified by chromVAR[64]. The top differential motifs were selected on the basis of the s.d. of the motif enrichment score. Motifs with similar sequences were collapsed into one motif through motif clustering[65]. Representative motifs in glioma cells and normal brain cells are shown in Extended Data Fig. 2.

Identification of CNAs

For scRNA-seq, we used the inferCNV package[16] to identify the CNV events in MGH240. We used myeloid cells and T cell clusters as reference cells. We used the argument '--denoise --HMM --cluster_by_groups' and set '--cutoff' to 0.1. For scATAC-seq, the number of reads that fell into different cytobands of chromosomes was calculated and normalized by sequencing depth. Regions on the blacklist were excluded. To avoid the considerable impact of short high-signal regions, we limited the relative read count to the 20–80% range by replacing values out of this range. The CNV estimation was performed for each cell compared to the oligodendrocyte cells.

Permutation tests between NPC ratio and proliferation scores and between genetic lesions and DNA methylation

To evaluate the significance with which genetic lesions were associated with alternate cell states, we first ranked tumors on the basis of their NPC ratio or proliferation score. We then assessed the frequency of each genetic event in the top 50 tumors compared to 50 tumors randomly selected from TCGA cohort. This random selection process was repeated 1,000 times to calculate the probability (*P* value) that the frequency of genetic events in the randomly selected group would be as high or higher than the top 50 tumors. Similarly, for the permutation test on DNA methylation, tumors were ranked by NPC ratio or proliferation score. We calculated the average DNA methylation level in the top 50 tumors and compared it to the average level in 50 tumors randomly selected from TCGA cohort. This random selection was performed 1,000 times to determine the probability (*P* value) that the average DNA methylation level in the randomly selected group would be as low or lower than the top 50 tumors.

Statistical analysis of *IFNA/B* and *CDKN2A* codeletion and other IFN-related gene deletions

To ascertain the prevalence of codeletion of *IFNA/B* and *CDKN2A*, we analyzed various cancer types within TCGA database. For each cancer type, we randomly selected 100 tumor samples and repeated this process 1,000 times to calculate the average codeletion frequency. A similar method was applied to assess the frequency of codeletion across different grades of IDH-mutant gliomas. Furthermore, to evaluate the statistical enrichment of deletions among other IFN-related genes (for example *IRF1*, *STAT1*, *SETD2* and *IFIT1*) within various grades of IDH-mutant gliomas, we randomly sampled different grades of IDH-mutant gliomas 1,000 times and computed the average deletion frequency of these IFN-related genes. Then, *t*-tests were conducted to assess the statistical differences in the average percentages for all examined conditions.

Identification of malignant cell-specific IFN signature

IFN signature genes were extracted from the gene set enrichment analysis (GSEA)[66] hallmarks gene database and clustered on the basis of their expression across malignant cells, oligodendrocytes, T cells and myeloid cells in scRNA-seq data for IDH-mutant gliomas (Extended Data Fig. 4c). Genes with the highest expression in malignant cells were integrated into a malignant cell-specific IFN signature. Gene set variation analysis (GSVA) scores for the original IFN signature and the malignant cell-specific IFN signature were calculated and compared.

DNA methylation analysis

The 450K DNA methylation data[15] of TCGA IDH-mutant gliomas was downloaded from UCSC Xena[67] and global DNA methylation levels were calculated across all probes in the matrix for each sample. We defined a set of methylation-sensitive genes using published data[68]. Here, we collated genes that were both hypomethylated and upregulated by treatment with DNMT1 inhibitor in a glioma cell line.

Gene enrichment variation score analysis

Bulk RNA-seq data for TCGA IDH-mutant gliomas were downloaded from UCSC Xena and the gene enrichment variation scores were calculated using the GSVA r package.

Quantification of transposable elements

Malignant cells from scRNA-seq data were identified and their raw reads were extracted by all reads and processed by SalmonTE to quantify the expression levels of each transposable element subfamily. The value of all retroelements in major categories (L1, SVA, LTR, ERV, Alu and MER) was summed.

Statistics and reproducibility

The sample size of ten tumors for our scATAC-seq experiments was based on prior scATAC-seq studies in glioma, where sample sizes of fewer than ten tumors were sufficient to capture overall patterns of chromatin accessibility across tumors[20,69]. No tumors were excluded in our analyses but cells not meeting quality control metrics described above were excluded. Tumor samples were collected prospectively without randomization or blinding procedures. The specific statistical tests used for the different analyses performed are described in the relevant sections above. Before statistical testing, data were analyzed to confirm that they met the assumptions of the statistical tests used.

Reporting summary

Further information on research design is available in the Nature Portfolio Reporting Summary linked to this article.

Data availability

Processed scATAC-seq and scRNA-seq data are available through the Gene Expression Omnibus under accession number GSE241745. Raw data are available through the dbGaP under accession number phs003697. The human glioma bulk RNA-seq and methylation data were obtained from TCGA Research Network (http://cancergenome.nih.gov/). All other data supporting the findings of this study are available from the corresponding author on reasonable request. Source data are provided with this paper.

Code availability

Original code for the analyses performed in this study was deposited on GitHub (https://github.com/BernsteinLab/IDH_mutant_gliomas_progression_2024).

References

1. Parsons, D. W. et al. An integrated genomic analysis of human glioblastoma multiforme. *Science* **321**, 1807–1812 (2008).
2. Miller, J. J. et al. Isocitrate dehydrogenase (IDH) mutant gliomas: a Society for Neuro-Oncology (SNO) consensus review on diagnosis, management, and future directions. *Neuro Oncol.* **25**, 4–25 (2023).

3. Louis, D. N. et al. The 2021 WHO classification of tumors of the central nervous system: a summary. *Neuro Oncol.* **23**, 1231–1251 (2021).
4. Dang, L. et al. Cancer-associated *IDH1* mutations produce 2-hydroxyglutarate. *Nature* **465**, 966 (2010).
5. Xu, W. et al. Oncometabolite 2-hydroxyglutarate is a competitive inhibitor of α-ketoglutarate-dependent dioxygenases. *Cancer Cell* **19**, 17–30 (2011).
6. Noushmehr, H. et al. Identification of a CpG island methylator phenotype that defines a distinct subgroup of glioma. *Cancer Cell* **17**, 510–522 (2010).
7. Turcan, S. et al. *IDH1* mutation is sufficient to establish the glioma hypermethylator phenotype. *Nature* **483**, 479–483 (2012).
8. Flavahan, W. A. et al. Insulator dysfunction and oncogene activation in IDH mutant gliomas. *Nature* **529**, 110–114 (2016).
9. Rahme, G. J. et al. Modeling epigenetic lesions that cause gliomas. *Cell* **186**, 3674–3685 (2023).
10. Fueyo, J. et al. Hypermethylation of the CpG island of p16/CDKN2 correlates with gene inactivation in gliomas. *Oncogene* **13**, 1615–1619 (1996).
11. Costello, J. F., Berger, M. S., Huang, H. S. & Cavenee, W. K. Silencing of p16/CDKN2 expression in human gliomas by methylation and chromatin condensation. *Cancer Res.* **56**, 2405–2410 (1996).
12. Lu, C. et al. IDH mutation impairs histone demethylation and results in a block to cell differentiation. *Nature* **483**, 474–478 (2012).
13. Notarangelo, G. et al. Oncometabolite D-2HG alters T cell metabolism to impair $CD8^+$ T cell function. *Science* **377**, 1519–1529 (2022).
14. Bunse, L. et al. Suppression of antitumor T cell immunity by the oncometabolite (*R*)-2-hydroxyglutarate. *Nat. Med.* **24**, 1192–1203 (2018).
15. Ceccarelli, M. et al. Molecular profiling reveals biologically discrete subsets and pathways of progression in diffuse glioma. *Cell* **164**, 550–563 (2016).
16. Tirosh, I. et al. Single-cell RNA-seq supports a developmental hierarchy in human oligodendroglioma. *Nature* **539**, 309–313 (2016).
17. Venteicher, A. S. et al. Decoupling genetics, lineages, and microenvironment in IDH-mutant gliomas by single-cell RNA-seq. *Science* **355**, eaai8478 (2017).
18. Wei, Y. et al. Stalled oligodendrocyte differentiation in IDH-mutant gliomas. *Genome Med.* **15**, 24 (2023).
19. Babikir, H. et al. ATRX regulates glial identity and the tumor microenvironment in IDH-mutant glioma. *Genome Biol.* **22**, 311 (2021).
20. Wang, L. et al. The phenotypes of proliferating glioblastoma cells reside on a single axis of variation. *Cancer Discov.* **9**, 1708–1719 (2019).
21. Yu, K. et al. Surveying brain tumor heterogeneity by single-cell RNA-sequencing of multi-sector biopsies. *Natl Sci Rev* **7**, 1306–1318 (2020).
22. Johnson, K. C. et al. Single-cell multimodal glioma analyses identify epigenetic regulators of cellular plasticity and environmental stress response. *Nat. Genet.* **53**, 1456–1468 (2021).
23. Chaligne, R. et al. Epigenetic encoding, heritability and plasticity of glioma transcriptional cell states. *Nat. Genet.* **53**, 1469–1479 (2021).
24. Trevino, A. E. et al. Chromatin and gene-regulatory dynamics of the developing human cerebral cortex at single-cell resolution. *Cell* **184**, 5053–5069 (2021).
25. Morabito, S. et al. Single-nucleus chromatin accessibility and transcriptomic characterization of Alzheimer's disease. *Nat. Genet.* **53**, 1143–1155 (2021).
26. Couturier, C. P. et al. Single-cell RNA-seq reveals that glioblastoma recapitulates a normal neurodevelopmental hierarchy. *Nat. Commun.* **11**, 3406 (2020).
27. Burdziak, C. et al. Epigenetic plasticity cooperates with cell–cell interactions to direct pancreatic tumorigenesis. *Science* **380**, eadd5327 (2023).
28. Yanchus, C. et al. A noncoding single-nucleotide polymorphism at 8q24 drives IDH1-mutant glioma formation. *Science* **378**, 68–78 (2022).
29. Cancer Genome Atlas Research Network et al. Comprehensive, integrative genomic analysis of diffuse lower-grade gliomas. *N. Engl. J. Med.* **372**, 2481–2498 (2015).
30. Varn, F. S. et al. Glioma progression is shaped by genetic evolution and microenvironment interactions. *Cell* **185**, 2184–2199 (2022).
31. Blanco-Carmona, E. et al. Tumor heterogeneity and tumor–microglia interactions in primary and recurrent IDH1-mutant gliomas. *Cell Rep. Med.* **4**, 101249 (2023).
32. Miller, T. E. et al. Programs, origins, and niches of immunomodulatory myeloid cells in gliomas. Preprint at *bioRxiv* https://doi.org/10.1101/2023.10.24.563466 (2023).
33. Barriga, F. M. et al. MACHETE identifies interferon-encompassing chromosome 9p21.3 deletions as mediators of immune evasion and metastasis. *Nat. Cancer* **3**, 1367–1385 (2022).
34. Chen, K. et al. Methyltransferase SETD2-mediated methylation of STAT1 is critical for interferon antiviral activity. *Cell* **170**, 492–506 (2017).
35. Jacob, F. et al. A patient-derived glioblastoma organoid model and biobank recapitulates inter- and intra-tumoral heterogeneity. *Cell* **180**, 188–2042 (2020).
36. Abdullah, K. G. et al. Establishment of patient-derived organoid models of lower-grade glioma. *Neuro Oncol.* **24**, 612–623 (2021).
37. Gorbunova, V. et al. The role of retrotransposable elements in ageing and age-associated diseases. *Nature* **596**, 43–53 (2021).
38. Mellinghoff, I. K. et al. Vorasidenib in IDH1- or IDH2-mutant low-grade glioma. *N. Engl. J. Med.* **389**, 589–601 (2023).
39. Mellinghoff, I. K. et al. Vorasidenib and ivosidenib in IDH1-mutant low-grade glioma: a randomized, perioperative phase 1 trial. *Nat. Med.* **29**, 615–622 (2023).
40. Spitzer, A. et al. Mutant IDH inhibitors induce lineage differentiation in IDH-mutant oligodendroglioma. *Cancer Cell* **42**, 904–914.e9 (2024).
41. Couturier, C. P. et al. Glioblastoma scRNA-seq shows treatment-induced, immune-dependent increase in mesenchymal cancer cells and structural variants in distal neural stem cells. *Neuro Oncol.* **24**, 1494–1508 (2022).
42. Giovannoni, F. & Quintana, F. J. The role of astrocytes in CNS inflammation. *Trends Immunol.* **41**, 805–819 (2020).
43. Rahme, G. J., Luikart, B. W., Cheng, C. & Israel, M. A. A recombinant lentiviral PDGF-driven mouse model of proneural glioblastoma. *Neuro Oncol.* **20**, 332–342 (2018).
44. Jun, H. J. et al. A PDGFRα-driven mouse model of glioblastoma reveals a stathmin1-mediated mechanism of sensitivity to vinblastine. *Nat. Commun.* **9**, 3116 (2018).
45. Goenka, A. et al. Oncogenic long noncoding RNA LINC02283 enhances PDGF receptor A-mediated signaling and drives glioblastoma tumorigenesis. *Neuro Oncol.* **25**, 1592–1604 (2023).
46. Ganz, J. et al. Rates and patterns of clonal oncogenic mutations in the normal human brain. *Cancer Discov.* **12**, 172–185 (2022).
47. Herman, J. G. et al. Inactivation of the *CDKN2/p16/MTS1* gene is frequently associated with aberrant DNA methylation in all common human cancers. *Cancer Res.* **55**, 4525–4530 (1995).
48. Gonzalez-Zulueta, M. et al. Methylation of the 5′ CpG Island of the *p16/CDKN2* tumor suppressor gene in normal and transformed human tissues correlates with gene silencing. *Cancer Res.* **55**, 4531–4535 (1995).

49. Kohanbash, G. et al. Isocitrate dehydrogenase mutations suppress STAT1 and CD8$^+$ T cell accumulation in gliomas. *J. Clin. Invest.* **127**, 1425–1437 (2017).
50. Amankulor, N. M. et al. Mutant IDH1 regulates the tumor-associated immune system in gliomas. *Genes Dev.* **31**, 774–786 (2017).
51. Chiappinelli, K. B. et al. Inhibiting DNA methylation causes an interferon response in cancer via dsRNA including endogenous retroviruses. *Cell* **162**, 974–986 (2015).
52. Hu, J. et al. STING inhibits the reactivation of dormant metastasis in lung adenocarcinoma. *Nature* **616**, 806–813 (2023).
53. Volkman, H. E., Cambier, S., Gray, E. E. & Stetson, D. B. Tight nuclear tethering of cGAS is essential for preventing autoreactivity. *eLife* **8**, e47491 (2019).
54. Fang, L. et al. Methionine restriction promotes cGAS activation and chromatin untethering through demethylation to enhance antitumor immunity. *Cancer Cell* **41**, 1118–1133 (2023).
55. Turcan, S. et al. Mutant-IDH1-dependent chromatin state reprogramming, reversibility, and persistence. *Nat. Genet.* **50**, 62–72 (2018).
56. Gierahn, T. M. et al. Seq-Well: portable, low-cost RNA sequencing of single cells at high throughput. *Nat. Methods* **14**, 395–398 (2017).
57. Satpathy, A. T. et al. Massively parallel single-cell chromatin landscapes of human immune cell development and intratumoral T cell exhaustion. *Nat. Biotechnol.* **37**, 925–936 (2019).
58. Azevedo Portilho, N. et al. The DNMT1 inhibitor GSK-3484862 mediates global demethylation in murine embryonic stem cells. *Epigenetics Chromatin* **14**, 56 (2021).
59. Kaminow, B., Yunusov, D. & Dobin, A. STARsolo: accurate, fast and versatile mapping/quantification of single-cell and single-nucleus RNA-seq data. Preprint at *bioRxiv* https://doi.org/10.1101/2021.05.05.442755 (2021).
60. Bravo González-Blas, C. et al. cisTopic: *cis*-regulatory topic modeling on single-cell ATAC-seq data. *Nat. Methods* **16**, 397–400 (2019).
61. Stuart, T., Srivastava, A., Madad, S., Lareau, C. A. & Satija, R. Single-cell chromatin state analysis with Signac. *Nat. Methods* **18**, 1333–1341 (2021).
62. Hao, Y. et al. Integrated analysis of multimodal single-cell data. *Cell* **184**, 3573–3587 (2021).
63. Kotliar, D. et al. Identifying gene expression programs of cell-type identity and cellular activity with single-cell RNA-Seq. *eLife* **8**, e43803 (2019).
64. Schep, A. N., Wu, B., Buenrostro, J. D. & Greenleaf, W. J. chromVAR: inferring transcription-factor-associated accessibility from single-cell epigenomic data. *Nat. Methods* **14**, 975–978 (2017).
65. Vierstra, J. et al. Global reference mapping of human transcription factor footprints. *Nature* **583**, 729–736 (2020).
66. Subramanian, A. et al. Gene set enrichment analysis: a knowledge-based approach for interpreting genome-wide expression profiles. *Proc. Natl Acad. Sci. USA* **102**, 15545–15550 (2005).
67. Goldman, M. J. et al. Visualizing and interpreting cancer genomics data via the Xena platform. *Nat. Biotechnol.* **38**, 675–678 (2020).
68. Turcan, S. et al. Efficient induction of differentiation and growth inhibition in IDH1 mutant glioma cells by the DNMT inhibitor decitabine. *Oncotarget* **4**, 1729–1736 (2013).
69. Guilhamon, P. et al. Single-cell chromatin accessibility profiling of glioblastoma identifies an invasive cancer stem cell population associated with lower survival. *eLife* **10**, e64090 (2021).
70. Barthel, F. P. et al. Longitudinal molecular trajectories of diffuse glioma in adults. *Nature* **576**, 112–120 (2019).
71. Neftel, C. et al. An integrative model of cellular states, plasticity, and genetics for glioblastoma. *Cell* **178**, 835–849 (2019).

Acknowledgements

We thank G. Rahme, C. Couturier, J. Verga, M. Thompsom and all members of the Bernstein laboratory for their discussions. We thank S. Ma, V. Kartha, C. Lareau and J. Buenrostro for guiding the scATAC-seq experiment and analysis. We thank S. Gritsch and D. Silverbush for providing help with the preparation and analysis of glioma samples. This work was supported by funds from the National Cancr Institute (NCI) and National Institutes of Health (NIH) Director's Fund (DP1CA216873 to B.E.B.) and the Ludwig Center at Harvard. J.W. was supported by a Damon Runyon postdoctoral fellowship award and King Trust fellowship award. L.N.G.C was supported by NIH award K12CA090354 and a Harold Amos faculty development award from the Robert Wood Johnson Foundation. B.E.B. is the Richard and Nancy Lubin Family Endowed Chair at the Dana-Farber Cancer Institute and an American Cancer Society research professor. This work was supported by grants to M.L.S. from the Mark Foundation (emerging leader award), the Sontag Foundation (distinguished scientist award), the MGH Research Scholars and NCI R37CA245523 and R01CA258763.

Author contributions

Conceptualization and experimental design, J.W., L.N.G.C., M.L.S. and B.E.B. Methodology and data acquisition, J.W., L.N.G.C., S.B., J.D.A. and T.E.M. Analysis and interpretation of data, J.W., L.N.G.C., C.A.E.F., M.L.S. and B.E.B. Manuscript writing and revision, J.W., L.N.G.C., M.L.S. and B.E.B.

Competing interests

L.N.G.C. has received research funding from Merck & Co. (to the Dana-Farber Cancer Institute) and has received consulting fees from Elsevier, Servier Laboratories, BMJ Best Practice, Prime Education and Oakstone Publishing. B.E.B. discloses financial interests in HiFiBio, Arsenal Biosciences, Chroma Medicine, Cell Signaling Technologies and Design Pharmaceuticals. M.L.S. discloses financial interests in Immunitas Therapeutics. T.E.M. discloses financial interest in Reify Health, Care Access Research and Telomere Diagnostics. The remaining authors declare no competing interests.

Additional information

Extended data is available for this paper at https://doi.org/10.1038/s43018-024-00865-3.

Supplementary information The online version contains supplementary material available at https://doi.org/10.1038/s43018-024-00865-3.

Correspondence and requests for materials should be addressed to Bradley E. Bernstein.

Peer review information *Nature Cancer* thanks Shi-Yuan Cheng, Roel Verhaak and the other, anonymous, reviewer(s) for their contribution to the peer review of this work.

https://doi.org/10.1038/s43018-024-00865-3

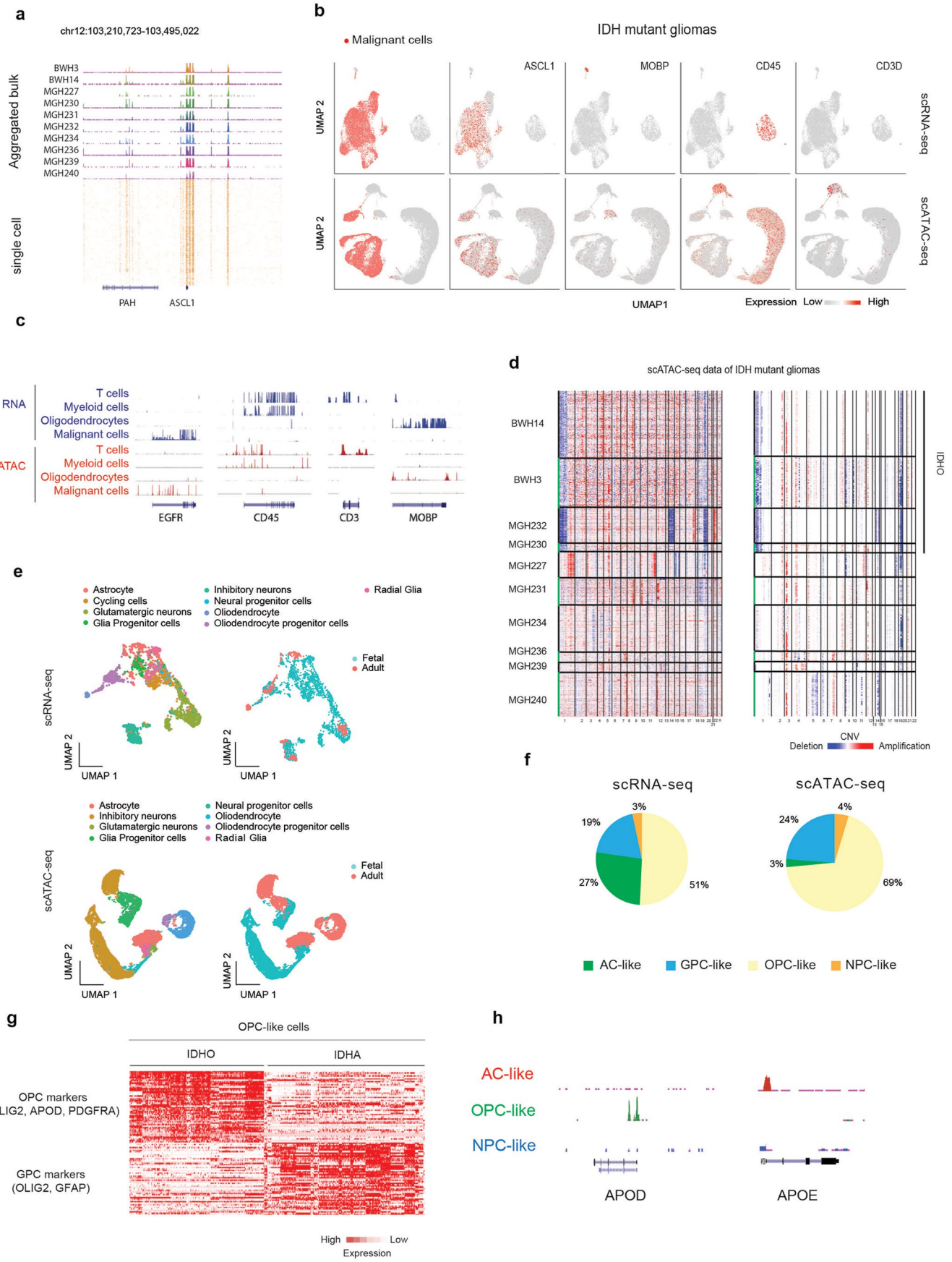

Extended Data Fig. 1 | See next page for caption.

https://doi.org/10.1038/s43018-024-00865-3

Extended Data Fig. 1 | Identification of malignant cells and their developmental states from scRNA-seq and scATAC-seq data. a. Genome tracks show aggregated (pseudo-bulk) scATAC-seq data for IDH-mutant gliomas (n=10) over a representative neural locus (*ASCL1*). **b**. UMAP visualization of IDH-mutant glioma cells profiled by scRNA-seq and scATAC-seq. The leftmost plots indicate annotated malignant cells, while the others depict expression or promoter and gene body accessibility (red) of cell type-specific genes. **c**. Genome tracks show aggregated scRNA-seq and scATAC-seq data over representative cell type-specific genes. **d**. CNAs inferred from scATAC-seq data for malignant cells from IDH-mutant cohorts used in this study (see Methods). CNAs inferred directly from the scATAC-seq data (right) were consistent with CNAs derived by applying inferCNV to imputed gene activity scores (left). **e**. UMAP visualizations of integrated scRNA-seq and scATAC-seq data from normal fetal and adult brain cells. Cells are colored by annotated cell types (left) and donor types (right). **f**. Pie charts depict the distributions of cell state annotations nominated by scRNA-seq (left) or scATAC-seq (right). **g**. Gene programs enriched in OPC-like cells from IDH-mutant oligodendrogliomas (IDH-O) or astrocytomas (IDH-A) by NMF analysis. **h**. Genome tracks show aggregated scATAC-seq data for each cell state over oligodendrocyte- (*APOD*) and astrocyte-specific (*APOE*) genes.

https://doi.org/10.1038/s43018-024-00865-3

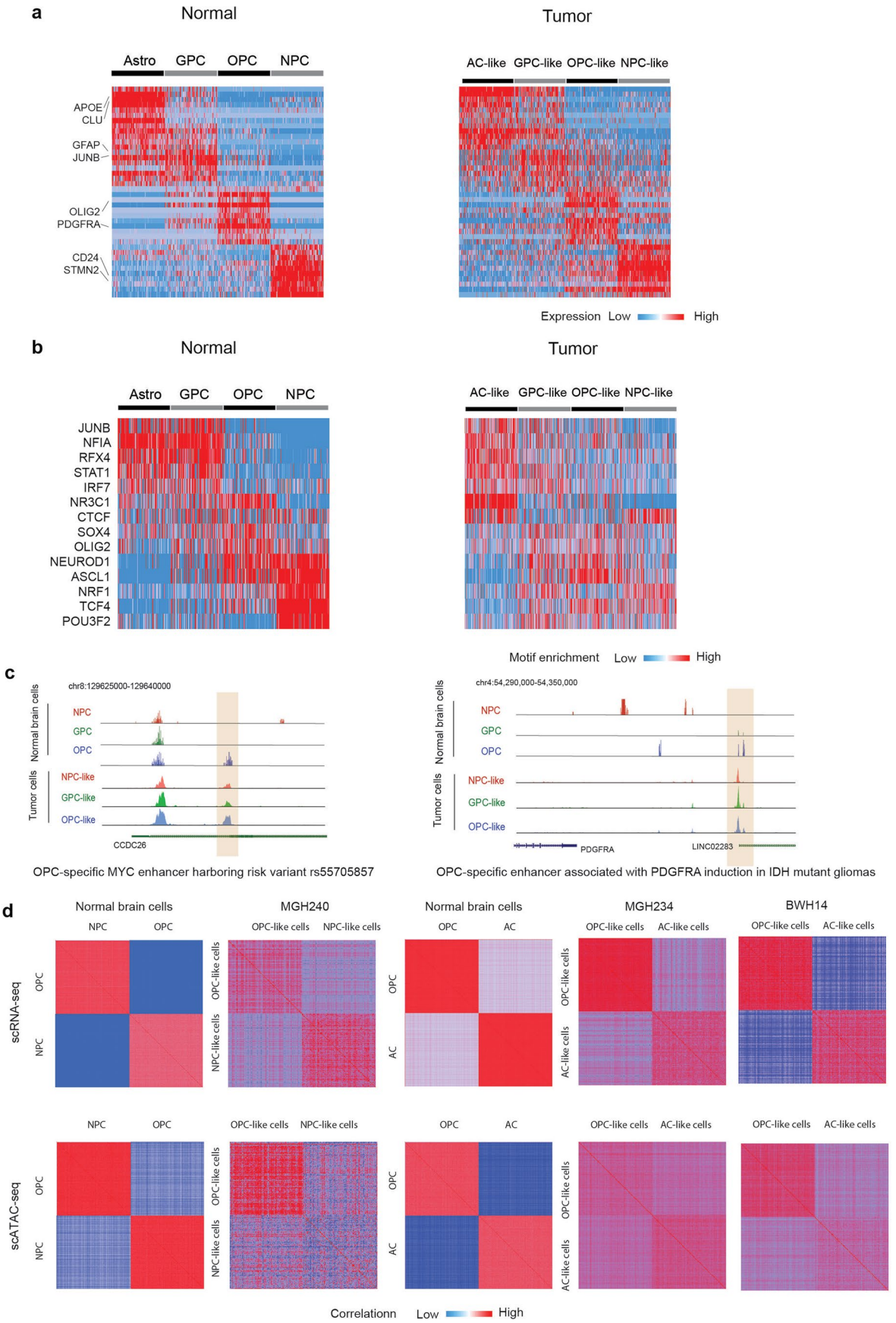

Extended Data Fig. 2 | See next page for caption.

https://doi.org/10.1038/s43018-024-00865-3

Extended Data Fig. 2 | Marker genes and TF motifs associated with glioma cell states. a. Heatmaps show the expression of variable genes (rows) across individual brain or malignant cells (columns). Cells are grouped by their assigned states. **b**. Heatmaps depict TF motif enrichments (rows) in scATAC-seq profiles for individual brain or malignant cells (columns). **c**. Genome tracks show aggregate accessibility over portions of the *MYC* and *PDGFRA* loci in normal brain and malignant glioma cell types. Shaded intervals correspond to an OPC-specific enhancer in the MYC locus that harbors a genetic variant associated with glioma risk (left) and an OPC-specific enhancer implicated in *PDGFRA* induction. **d**. Heatmaps show pairwise correlations of scRNA-seq (top) or scATAC-seq (bottom) data for normal brain cells or malignant glioma cells grouped by their cell type classifications, as in Fig. 2c, but with data from three high-grade IDH-mutant gliomas with matched scRNA-seq and scATAC-seq data.

https://doi.org/10.1038/s43018-024-00865-3

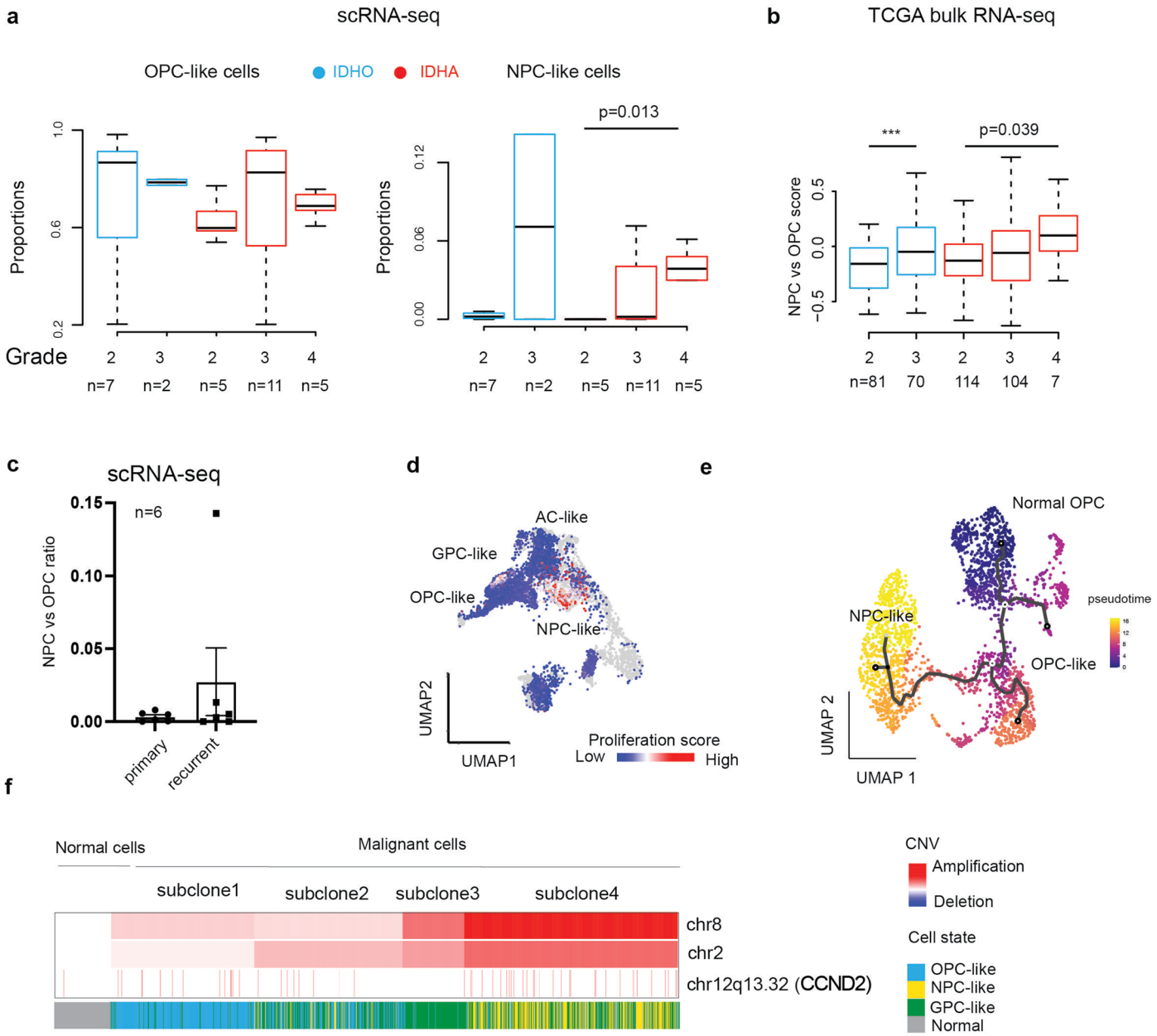

Extended Data Fig. 3 | Glioma progression associated with increasing proportions of NPC-like cells. a. Box plots depict proportions of OPC-like and NPC-like cells in IDH-mutant gliomas, stratified by grade and subtype (n=7 for IDHO grade 2, n=2 for IDHO grade 3, n=5 for IDHA grade 2, n=11 for IDHA grade 3, n=5 for IDHA grade 4). Boxes depict 25th, 50th and 75th percentiles, and whiskers depict extreme values. One-tailed t-test P-value: 0.013 for NPC-like proportions. **b.** Box plots depict relative proportions of NPC-like versus OPC-like cells, inferred from bulk expression data for IDH-mutant gliomas (TCGA), stratified by grade and subtype (n=81 for IDHO grade 2, n=70 for IDHO grade 3, n=114 for IDHA grade 2, n=104 for IDHA grade 3, n=7 for IDHA grade 4). One-tailed t-test P-value: 0.039; *** defines p<0.001. **c.** Barplot depicts the ratio of NPC-like to OPC-like cells in scRNA-seq data for six matched pairs of primary and recurrent tumors. Data are presented as mean values +/- SEM. **d.** UMAP visualization of malignant cells projected onto normal brain cells, as in Figs. 1b and 3a, with heat depicting the proliferation scores of individual malignant cells. **e.** Trajectory analysis was performed on combined scRNA-seq data for malignant cells and normal OPCs, using the Monocle package. The pseudotime coloring and best-fit trajectory are consistent with progression from normal OPC to OPC-like and then NPC-like malignant cells. **f.** Plot depicts CNAs for loci subject to CNAs (rows) across single cells (columns) from a second IDH-mutant glioma (OPK438), as in Fig. 3g. Malignant cells are grouped into subclones based on CNAs, and compared to normal cells from the same resection (left). Malignant cell state assignments indicated.

https://doi.org/10.1038/s43018-024-00865-3

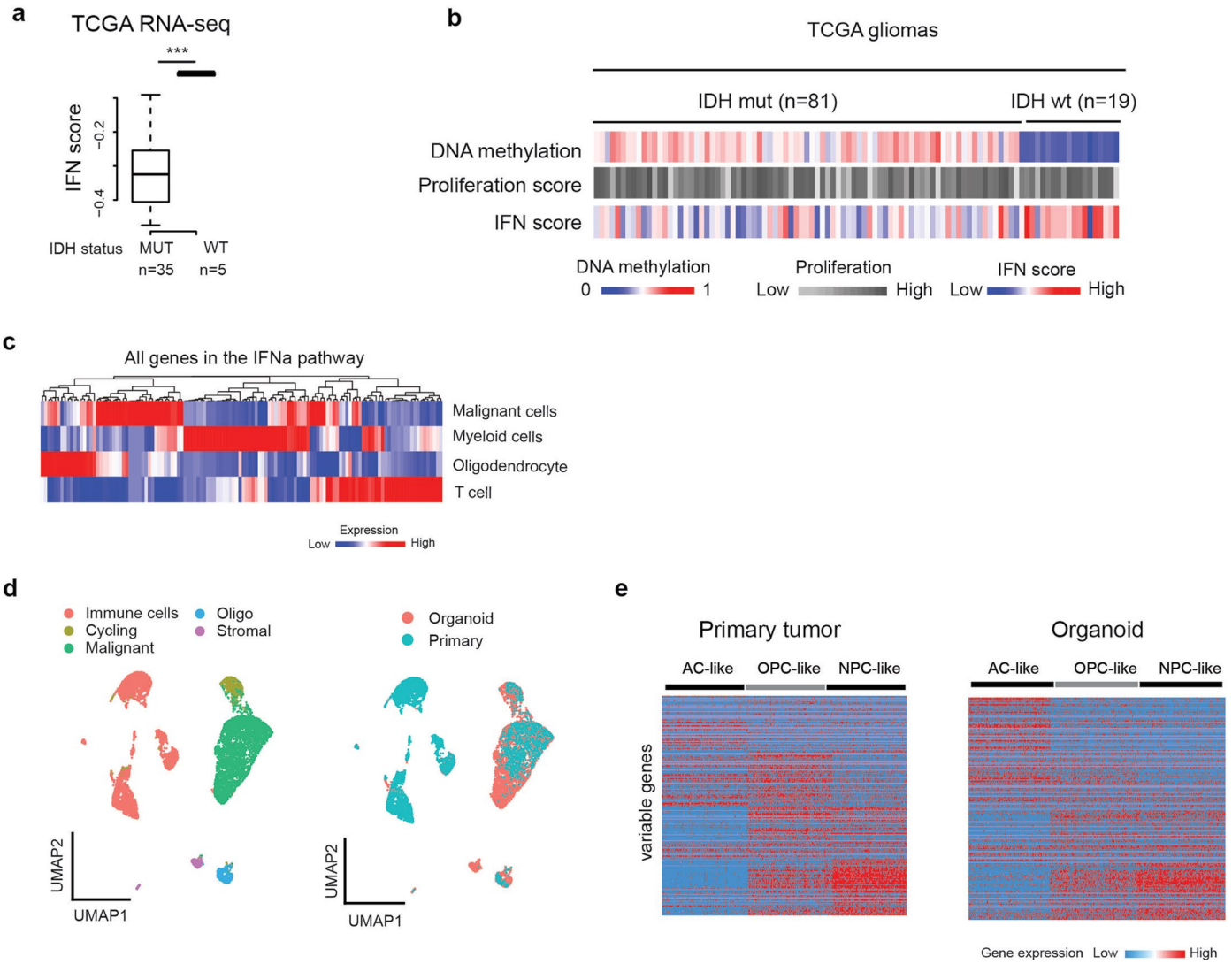

Extended Data Fig. 4 | Validation of IFN signature in malignant cells and glioma organoids. a. Boxplot depicts IFN signature scores (RNA-seq) for grade 2 IDH mutant and WT gliomas (n=35 for IDH mutant and n=5 for IDH WT) with high purity estimates (>80%). Boxes depict 25th, 50th and 75th percentiles, and whiskers depict extreme values. One-tailed t-test P-values: *** defines p<0.001. **b**. Heatmap shows DNA methylation levels, proliferation scores, and IFN scores (rows) in grade 2 IDH-mutant and grade 2 IDH WT TCGA gliomas (columns) based on the 2016 WHO classification. **c**. Heatmap depicts the expression of IFN pathway genes (columns) clustered by their expression across malignant cells, immune cell lineages, and oligodendrocytes (rows). This analysis distinguished malignant cell-specific IFN-related genes. **d**. UMAP visualization of scRNA-seq data compares cells from a glioma organoid (red) and the primary tumor from which it was derived (blue). **e**. Heatmaps depict the expression of variable genes associated with different cell states (rows) in single cells (columns) grouped by nominal cell identity. The glioma organoids recapitulate cell types and transcriptional programs as seen in the primary tumors.

https://doi.org/10.1038/s43018-024-00865-3

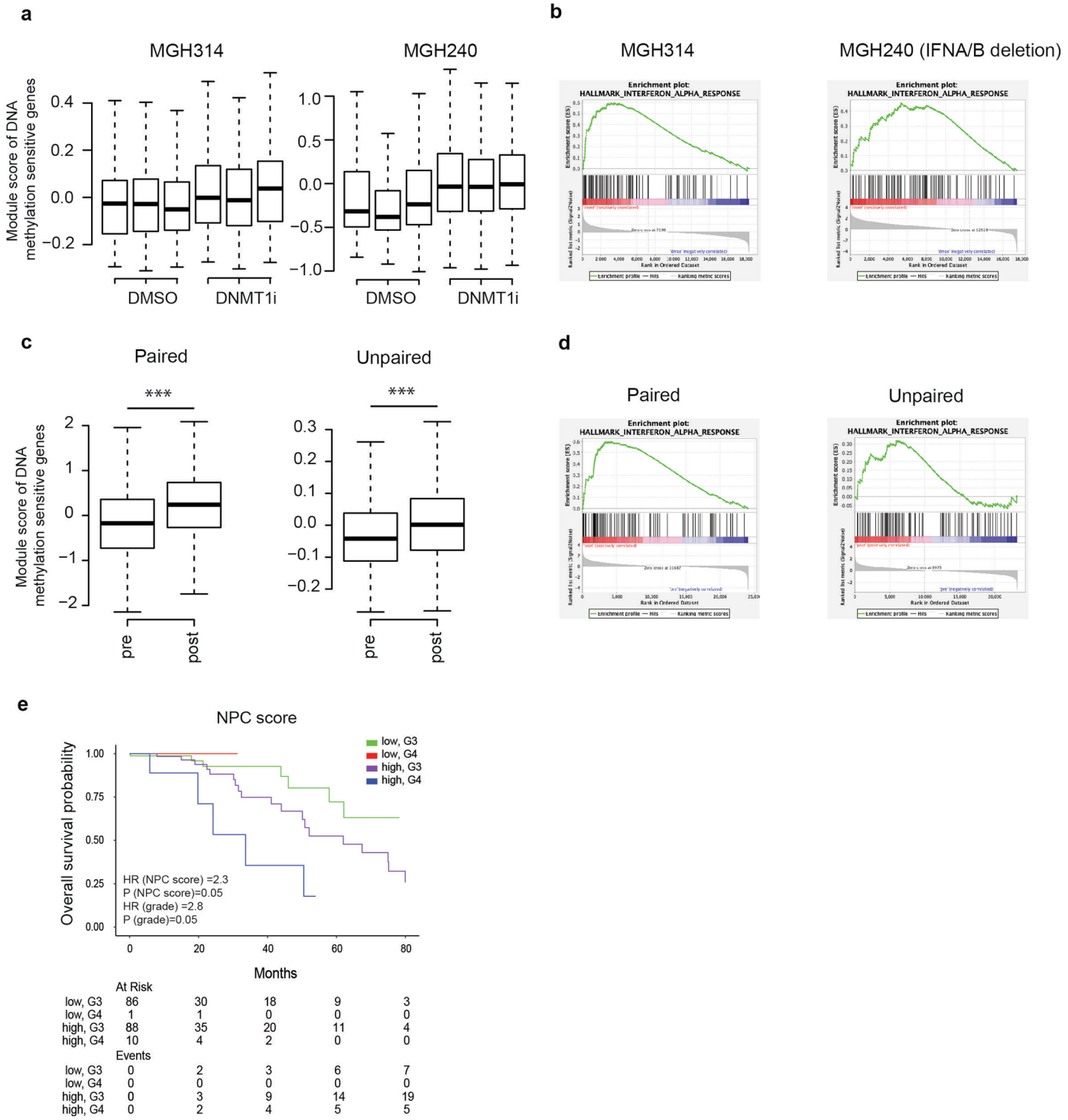

Extended Data Fig. 5 | IFN genes are upregulated by DNMT1 and IDH inhibitors. a. Box plots depict module scores (Seurat) for gene correlates of DNA methylation loss in IDH-mutant glioma organoids treated with DNMT1 inhibitor or control (n=3 technical replicates). Boxes depict 25th, 50th and 75th percentiles, and whiskers depict extreme values. **b**. Running Enrichment Score (GSEA) for IFNa genes regulated by DNMT1 inhibitor. **c**. Box plots depict module scores (Seurat) for gene correlates of methylation loss in IDH-mutant gliomas resected from patients treated with IDH inhibitors. Left: paired pre- and post-treatment samples from a single patient. Right: unpaired samples from 6 untreated and 2 treated patients. Two-tailed t-test P values: ***p<0.001. **d**. Running Enrichment Score (GSEA) for IFNa genes in IDH-mutant gliomas resected from patients treated with IDH inhibitor (as in c). **e**. Multivariate survival analysis for high-grade IDH-mutant gliomas (grade 3 and 4) stratified by NPC enrichment score and tumor grade. Hazard ratios (HR) and P-value associated with NPC-enriched tumors are indicated.

nature portfolio

Corresponding author(s): Bradley E. Bernstein

Last updated by author(s): Sep 22, 2024

Reporting Summary

Nature Portfolio wishes to improve the reproducibility of the work that we publish. This form provides structure for consistency and transparency in reporting. For further information on Nature Portfolio policies, see our Editorial Policies and the Editorial Policy Checklist.

Statistics

For all statistical analyses, confirm that the following items are present in the figure legend, table legend, main text, or Methods section.

n/a	Confirmed
☐	☒ The exact sample size (*n*) for each experimental group/condition, given as a discrete number and unit of measurement
☐	☒ A statement on whether measurements were taken from distinct samples or whether the same sample was measured repeatedly
☐	☒ The statistical test(s) used AND whether they are one- or two-sided *Only common tests should be described solely by name; describe more complex techniques in the Methods section.*
☒	☐ A description of all covariates tested
☒	☐ A description of any assumptions or corrections, such as tests of normality and adjustment for multiple comparisons
☐	☒ A full description of the statistical parameters including central tendency (e.g. means) or other basic estimates (e.g. regression coefficient) AND variation (e.g. standard deviation) or associated estimates of uncertainty (e.g. confidence intervals)
☐	☒ For null hypothesis testing, the test statistic (e.g. *F*, *t*, *r*) with confidence intervals, effect sizes, degrees of freedom and *P* value noted *Give P values as exact values whenever suitable.*
☒	☐ For Bayesian analysis, information on the choice of priors and Markov chain Monte Carlo settings
☒	☐ For hierarchical and complex designs, identification of the appropriate level for tests and full reporting of outcomes
☒	☐ Estimates of effect sizes (e.g. Cohen's *d*, Pearson's *r*), indicating how they were calculated

Our web collection on statistics for biologists contains articles on many of the points above.

Software and code

Policy information about availability of computer code

Data collection	TCGA data were downloaded from UCSC Xena; scRNA-seq data were downloaded from GEO
Data analysis	STARsolo, CellRanger ATAC, R-3.6, Bedtools, Samtools, Signac, cisTopic, Seurat, cNMF, chromVAR, inferCNV, GSEA, GSVA, SalmonTE

For manuscripts utilizing custom algorithms or software that are central to the research but not yet described in published literature, software must be made available to editors and reviewers. We strongly encourage code deposition in a community repository (e.g. GitHub). See the Nature Portfolio guidelines for submitting code & software for further information.

Data

Policy information about availability of data

All manuscripts must include a data availability statement. This statement should provide the following information, where applicable:

- Accession codes, unique identifiers, or web links for publicly available datasets
- A description of any restrictions on data availability
- For clinical datasets or third party data, please ensure that the statement adheres to our policy

Processed data are available through the Gene Expression Omnibus (GEO) under accession number GSE241745; Raw data are available through the dbGaP under accession no. phs003697.

Research involving human participants, their data, or biological material

Policy information about studies with human participants or human data. See also policy information about sex, gender (identity/presentation), and sexual orientation and race, ethnicity and racism.

Reporting on sex and gender	Patients includes both male and female; Age from 24-45
Reporting on race, ethnicity, or other socially relevant groupings	Race, ethnicity or other social groupings were not relevant for the purposes of our study, and as such, there was no selection for these and these data were not collected.
Population characteristics	The tumors analyzed in our study were sourced from adult patients (age range 24-45) with a diagnosis of IDH-mutant glioma, spanning grades 2-4
Recruitment	Tumor samples were obtained from IDH-mutant glioma patients undergoing clinically warranted surgical resection at MGH or BWH. The patients were consented to participate and have the data published by their neuro-oncologists to donate tumor samples for research under the auspices of Dana-Farber/Harvard Cancer Center Institutional Review Board Protocol 10-417
Ethics oversight	Patients consented to the use of their tumor samples for research under Dana-Farber/Harvard Cancer Center Institutional Review Board Protocol 10-417

Note that full information on the approval of the study protocol must also be provided in the manuscript.

Field-specific reporting

Please select the one below that is the best fit for your research. If you are not sure, read the appropriate sections before making your selection.

☒ Life sciences ☐ Behavioural & social sciences ☐ Ecological, evolutionary & environmental sciences

For a reference copy of the document with all sections, see nature.com/documents/nr-reporting-summary-flat.pdf

Life sciences study design

All studies must disclose on these points even when the disclosure is negative.

Sample size	The sample size of 10 tumors for our scATAC-seq cohort was based on the experience of prior studies applying scATAC-seq in glioma (PMID 33427645 and PMID 31554641), where sample sizes of 4 and 8 tumors, respectively, were sufficient to characterize consistent patterns of chromatin accessibility across tumors.
Data exclusions	No tumors were excluded in our analysis but individual cells not meeting QC metrics were excluded
Replication	For scATAC-seq data of tumors, we have 10 tumors as biological replicates. For scRNA-seq data of organoids, we have 3 technical replicates for each treatment experiment.
Randomization	not applicable
Blinding	not applicable

Reporting for specific materials, systems and methods

We require information from authors about some types of materials, experimental systems and methods used in many studies. Here, indicate whether each material, system or method listed is relevant to your study. If you are not sure if a list item applies to your research, read the appropriate section before selecting a response.

Materials & experimental systems

n/a	Involved in the study
☐	☒ Antibodies
☒	☐ Eukaryotic cell lines
☒	☐ Palaeontology and archaeology
☒	☐ Animals and other organisms
☒	☐ Clinical data
☒	☐ Dual use research of concern
☒	☐ Plants

Methods

n/a	Involved in the study
☒	☐ ChIP-seq
☐	☒ Flow cytometry
☒	☐ MRI-based neuroimaging

Antibodies

Antibodies used	Antibody was used for FACS: CD45- VioBlue (Miltenyi Biotec 130-113-122; 1:50 diltulted)
Validation	We only used commercially available antibodies. Validation experiments for the antibodies used can be found on the respective manufacturer's website: CD45- VioBlue (Miltenyi Biotec 130-113-122) https://www.miltenyibiotec.com/US-en/products/cd45-antibody-anti-human-reafinity-rea747.html#conjugate=vioblue:size=100-tests-in-200-ul

Plants

Seed stocks	NA
Novel plant genotypes	NA
Authentication	NA

Flow Cytometry

Plots

Confirm that:

☒ The axis labels state the marker and fluorochrome used (e.g. CD4-FITC).

☒ The axis scales are clearly visible. Include numbers along axes only for bottom left plot of group (a 'group' is an analysis of identical markers).

☒ All plots are contour plots with outliers or pseudocolor plots.

☒ A numerical value for number of cells or percentage (with statistics) is provided.

Methodology

Sample preparation	Tumor cells were blocked in 1% bovine serum albumin in Hanks buffered saline solution (BSA / HBSS). Tumors were first stained with CD45- Vioblue direct antibody conjugate (Miltenyi Biotec) for 30 min at 4C. Cells were washed with cold PBS and then re-suspended in 1 mL of BSA / HBSS containing 1 mM calcein AM (Life Technologies) and 0.33 mM TO-PRO-3 iodide (Life Technologies) to co-stain for 30 min before sorting.
Instrument	Beckton Dickson FACS Aria Fusion Special Order System (serial No P65828200003)
Software	BD FACSDiva 8.0.1
Cell population abundance	The number of viable CD45- cells sorted for downstream analyses varied by experiment as a function of tumor sample size and delay since the time of harvesting and sorting.
Gating strategy	Sorting was performed with the FACS Aria Fusion Special Order System (Becton Dickinson) using 488 nm (calcein AM, 530/30 filter), 640nm (TO-PRO-3, 670/14 filter), and 405 nm (CD45-VioBlue, 450/50 filter) lasers. Standard, strict forward scatter height versus area criteria was used to discriminate doublets and gate-only singleton cells. Viable single cells were identified as calcein AM positive and TO-PRO-3 negative.

☒ Tick this box to confirm that a figure exemplifying the gating strategy is provided in the Supplementary Information.